Understanding Interactions between Terrestrial Water and Carbon Cycles Using Integrated SMAP Soil Moisture and OCO-2 SIF Observations and Land Surface Models

Zhijiong Cao[1], Yongkang Xue[12]*, Hara Prasad Nayak[1], Dennis P. Lettenmaier[1], Christian Frankenberg[34], Philipp Köhler[5], and Ziwei Li[1].

[1]Department of Geography, University of California, Los Angeles, CA, USA.

[2]Department of Atmospheric and Oceanic Sciences, University of California, Los Angeles, CA, USA.

[3]Division of Geological and Planetary Sciences, California Institute of Technology, Pasadena, CA, USA.

[4]Jet Propulsion Laboratory, California Institute of Technology, Pasadena, CA, USA.

[5]Remote Sensing and Products Division at EUMETSAT, Darmstadt, Germany

Corresponding author: Yongkang Xue (yxue@geog.ucla.edu)

Key Points:

- Dynamic vegetation processes substantially improve of terrestrial carbon flux simulation.
- Satellite products lead to advances in simulation and understanding of water and carbon cycles and their interactions.
- The B parameter, representing the slope of water retention curve, shows the most significant effects on both water and carbon cycles.

Abstract

Recently, more advanced synchronous global-scale satellite observations, the Soil Moisture Active Passive enhanced Level 3 (SMAP L3) soil moisture product and the Orbiting Carbon Observatory 2 (OCO-2) solar-induced chlorophyll fluorescence (SIF) product, provide an opportunity to improve the simulations of both water and carbon cycles in land surface modeling. This study introduces a mechanistic representation of SIF to the Simplified Simple Biosphere Model version 4 (SSiB4) coupled with the Top-down Representation of Interactive Foliage and Flora Including Dynamics Model (TRIFFID). This newly developed model with the observed satellite data indicates that introducing dynamic processes can lead to substantial improvement in global carbon flux simulation. In the SSiB4/TRIFFID/SIF, four critical soil and vegetation parameters--B parameter, soil hydraulic conductivity at saturation (K_s), wilting point, and maximum Rubisco carboxylation rate (V_{max})--were identified through numerical sensitivity experiments. Among the four parameters, the B parameter has the most significant effects on both soil moisture and SIF simulations. With the optimized B parameter, both soil moisture and SIF simulations were improved substantially, with especially significant improvement for shrubs. The K_s and wilting point also affect both soil moisture and SIF but with reduced magnitude. The V_{max} directly affects photosynthesis, and its modification can substantially improve the SIF simulation of needleleaf trees and C_3 grasses. With all four calibrated parameters based on SMAP L3 and OCO-2 data, the root-mean-squared error (RMSE) of soil moisture and SIF simulations decreased from 0.076 to 0.063 m^3/m^3 and from 0.143 to 0.117 $W/m^2/\mu m/sr$, respectively.

1 Introduction

The terrestrial carbon and water cycles are tightly coupled by biological plant processes (Niyogi and Xue, 2006; Scholze et al., 2016). The interactions between soil moisture and carbon flux have been confirmed by previous studies (Koster et al., 2016; Qiu et al., 2018). Surface soil moisture plays a crucial role in land-atmosphere interactions (Humphrey et al., 2021; McColl et al., 2017; Seneviratne et al., 2010). It directly affects the photosynthesis and transpiration processes (Cox et al., 2002; Zhan et al., 2003) and indirectly affects carbon assimilation through

modulating phenological processes (Zhang et al., 2015). The amount of available soil moisture is a key limiting factor on photosynthesis and transpiration since it affects both the water use and carbon uptake of the plant through the leaf stomata gas exchange (Manzoni et al., 2013), which makes the interactions between vegetation and soil moisture dynamics contribute significantly to the structure and function in arid and semiarid ecosystems (Walker et al., 1981; Bhark and Small, 2003; D'Odorico et al., 2007). The terrestrial ecosystem provides feedback on the water cycle through transpiration and vegetation structure (Xue et al., 2004; Kang et al., 2007).

Surface soil moisture has large uncertainty in spatiotemporal distribution, and great efforts have been devoted to improving measurements using active or passive microwave instruments (Font et al., 2001; Njoku et al., 2003; Entekhabi et al., 2010; Kerr et al., 2012). The assimilation of the remotely sensed surface soil moisture has the potential to improve land surface processes modeling (Wander et al., 2014; Scholze et al., 2016). Wu et al. (2020) found that the Soil Moisture and Ocean Salinity (SMOS) soil moisture data can be used to constrain the simulations of the terrestrial biosphere carbon cycle to optimize soil hydrological and biophysical parameters simultaneously. The Soil Moisture Active Passive (SMAP) mission is the most recent space-borne mission at L-band and has been considered one of the most promising satellites for surface soil moisture monitoring (Wigneron et al., 2017). Recent studies suggest that SMAP outperforms other satellite products compared to in situ soil moisture measurements (Ma et al., 2019; Beck et al., 2021). Zhang et al. (2022) used the direct insertion of SMAP soil moisture observation to improve the simulated land-surface carbon fluxes across a variety of timescales. The SMAP product can provide a better representation of soil moisture, which suggests its potential for improvement in coupled carbon-water dynamics in terrestrial ecosystem models.

In recent years, remote sensing of solar-induced chlorophyll fluorescence (SIF) has been a rapidly advancing front in investigating carbon dynamics and other applications (Frankenberg et al., 2011; Sun et al., 2018; Doughty et al., 2022; Leng et al., 2022). The SIF retrieved from spaceborne spectrometers has been extensively used as a proxy for terrestrial photosynthesis to understand terrestrial ecosystem dynamics (Sun et al., 2017; Helm et al., 2020). As a signal emitted by the photochemically active centers of plants, SIF is directly linked to the actual process of photosynthesis (Porcar-Castell et al., 2014). Gonsamo et al. (2019) found that the Orbiting Carbon Observatory-2 (OCO-2) SIF can accurately capture the control of soil moisture

on photosynthetic activity, especially for regions with distinct seasonality of rainfall. Lee et al. (2015) incorporated equations coupling SIF to photosynthesis in a land surface model and confirmed that SIF has the potential to improve photosynthesis simulation. Qiu et al. (2018) incorporated this mechanistic representation of SIF and the Greenhouse gases Observing SATellite (GOSAT) and the Global Ozone Monitoring Experiment-2 (GOME-2) SIF measurements into a global terrestrial biosphere model, the Simplified Simple Biosphere Model version 2 (SSiB2/SIF), to evaluate and investigate the model-simulated relationships between soil moisture and SIF. In this study, we incorporated this existing SIF module into SSiB version 4 (SSiB4) to enable the fluorescence simulation, which is directly linked to photosynthetic activity and gross primary production (GPP).

In most studies, the vegetation conditions are specified based on observed and satellite-derived data, which suppresses the interactions between soil moisture and carbon cycle dynamics and indicates an important deficiency in the representation of terrestrial carbon processes in coupled carbon balance-based dynamic vegetation models. Dynamic vegetation models (DVMs) can simulate vegetation establishment, growth, competition, and mortality (Sitch et al., 2008). Studies suggest that the DVMs can be used at seasonal/interannual/decadal scales to simulate the land/atmosphere feedback (Lu et al., 2001; Levis and Bonan, 2004; Kim and Wang, 2012; Zhang et al., 2021). The Top-down Representation of Interactive Foliage and Flora Including Dynamics model (TRIFFID) uses the CO_2 fluxes at the land-atmosphere interface to update plant distributions and soil carbon, which allows the changes in biophysical properties to provide feedback onto the atmosphere (Cox et al., 2001; Hawkins et al., 2019). TRIFFID has been validated across spatial scales and ecosystems (Cox et al., 2000; Cox et al., 2004; Piao et al., 2009; Zhang et al., 2015; Liu et al., 2019). It serves as the foundation of the Joint UK Land Environment Simulator (JULES) for global carbon budget assessment (Clark et al., 2011; Le Quéré et al., 2016) and was coupled to SSiB4 to study the connections between vegetation dynamics and climate variability (Zhang et al., 2015). Liu et al. (2019) validated the vegetation distribution and leaf area index (LAI) simulated by SSiB4/TRIFFID against satellite products. With the coupling of TRIFFID, the relevant land-surface characteristics of vegetation cover and structure are modeled directly, which suggests SSiB4/TRIFFID can be used to investigate the role and mechanisms of the interactions between soil moisture and carbon cycle dynamics.

This study used the SMAP L3 soil moisture data, in conjunction with the OCO-2 SIF measurements, to evaluate the soil moisture and SIF simulated by SSiB2/SIF and SSiB4/TRIFFID/SIF as well as the relationships between the soil moisture and SIF simulation to investigate the effects of dynamic vegetation processes on soil moisture and carbon flux estimates. We integrated the two satellite measurements into SSiB4/TRIFFID/SIF to improve the model parameterization and to investigate the broad-scale relationships between soil moisture and carbon cycle dynamics, providing the opportunity to better understand the mechanistic processes in the global terrestrial biosphere model that bridges water and carbon cycles. This paper is organized as follows: Section 2 presents the model structure, experimental design, and the satellite datasets used for evaluation and calibration. The effects of the dynamic vegetation processes and key parameters on SM, SIF, and GPP simulations and the performance after calibration are illustrated in Section 3. Discussions and concluding remarks are presented in Section 4 and Section 5, respectively.

2 Model description, experimental design, and data

2.1 Model description

SSiB is a biosphere model that intends to simulate the biophysical exchange processes realistically (Xue et al., 1991 and 1996). Zhan et al. (2003) developed an analytical solution approach from a photosynthesis model (Collatz et al., 1991, 1992) and incorporated it into SSiB to generate SSiB2, which improved the land surface CO_2 fluxes simulation. The dynamic vegetation model, TRIFFID, which has been widely used in vegetation-climate interaction studies (Cox et al., 2000; Harper et al., 2016), was coupled to SSiB4 (Xue et al., 2006) to calculate vegetation dynamics. In SSiB4/TRIFFID, SSiB4 provides net plant photosynthesis assimilation rate, autotrophic respiration, and other surface conditions such as canopy temperature and soil moisture for TRIFFID. TRIFFID updates the vegetation dynamics, including the plant functional type (PFT) fractional coverage, vegetation height, and LAI, for SSiB4. Equations coupling SIF to photosynthesis, which were incorporated into the Community Land Model version 4 (CLM4, Lee et al., 2015), were incorporated into SSiB2 by Qiu et al.

(2018). In this study, the SIF module was incorporated into SSiB4/TRIFFID, forming SSiB4/TRIFFID/SIF, to enable the chlorophyll fluorescence simulation in photosynthesis.

2.2 Experimental design

In this study, SSiB2/SIF and SSiB4/TRIFFID/SIF were used to simulate the global soil moisture, SIF, and GPP and to assess the effects of the dynamic vegetation process on the simulations. The SSiB2/SIF model was driven by atmospheric forcing from 2010 to 2019 (Figure 1a). For the SSiB4/TRIFFID/SIF model, we first conducted spin-up simulations driven with climatological forcing and 1979 CO_2 concentration for 100 years to reach a quasi-equilibrium state as done by Liu et al. (2019) and Huang et al. (2020). Using the quasi-equilibrium simulation results as the initial vegetation conditions, such as each plant functional type's (PFT) fraction coverage, leaf area index (LAI), etc., we performed transient runs driven with historical meteorological forcing and yearly updated atmospheric CO_2 concentration from 1979 to 2019 (Liu et al., 2019) (Figure 1b). The time step of model integration is 3 h, and the spatial resolution of the model is 0.5°×0.5°. The experiments covered the period from 2010 to 2019 in SSiB2/SIF and 1979 to 2019 in SSiB4/TRIFFID/SIF, and the results from April 2015 to

December 2019, when the soil moisture and SIF satellite data were both available, were analyzed.

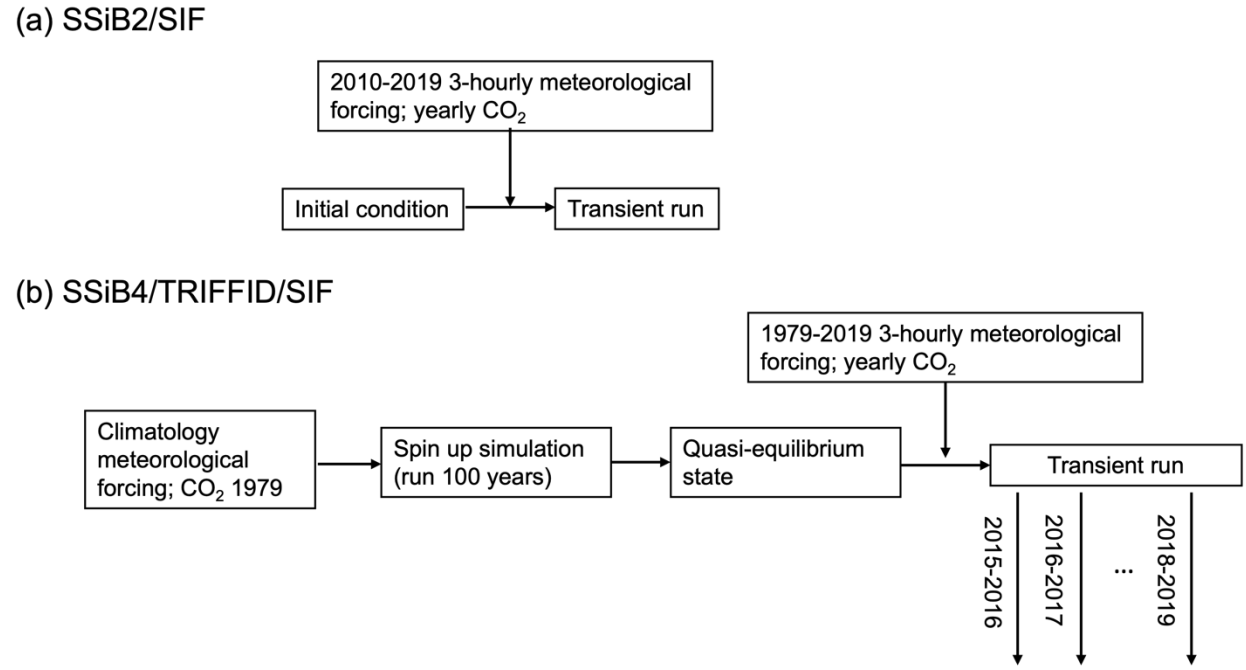

Figure 1. Experiment design for (a) SSiB2/SIF and (b) SSiB4/TRIFFID/SIF.

Studies have shown that soil properties substantially impact the soil moisture simulation in SSiB models, especially the parameterization of two key parameters, the B parameter and the hydraulic conductivity at saturation (K_s) (Xue et al., 1996; Qiu et al., 2018). The B parameter is an empirical constant that is dependent on the soil type. It represents the slope of the water retention curve and determines the relationship between the soil water potential and the volumetric soil water content through the following pedotransfer functions (Clapp and Hornberger, 1978):

$$\psi = \psi_s \left(\frac{\theta}{\theta_s}\right)^{-B} \quad (1)$$

where ψ is the soil water potential; ψ_s is the soil water potential at saturation; θ is the volumetric soil water content; and θ_s is the volumetric soil water content at saturation. The hydraulic conductivity at saturation (K_s) is the key coefficient in the soil water diffusion equation. This

equation is used to calculate the transfer of water between the three soil layers in SSiB models. Both the B parameter and K_s affect the soil water diffusion (Xue et al., 1996):

$$Q = -K_s \left(\frac{\theta}{\theta_s}\right)^{(2B+3)} \left[\frac{\partial \psi}{\partial Z} + 1\right] \quad (2)$$

where Q is the soil water diffusion; and $\partial\psi/\partial Z$ is the soil water potential gradient.

In addition to these two parameters, Qiu et al. (2018) found that the wilting point is a parameter directly linked to stomatal resistance and consequently to photosynthesis processes, thus affecting soil moisture through transpiration and demonstrating the close link between the water and carbon cycles. The wilting point is defined as the soil water content below which the vegetation transpiration process tends to inhibit (Tolk, 2003). In the SSiB model, an empirical equation was developed to relate the soil moisture and stomatal conductance for each PFT (Xue et al., 1991), in which the wilting point is the natural logarithm of soil water potential at which the stomata close completely. In SSiB2/SIF and SSiB4/TRIFFID/SIF, the wilting point controls the stomata opening and affects the photosynthesis process through the β factor, the adjustment parameter on stomatal conductance:

$$\beta = 1 - \exp\{-C_2[C_1 - \ln(-\psi)]\} \quad (3)$$

where C_1 is the wilting point and C_2 is a slope factor that depends on the vegetation type.

The maximum Rubisco carboxylation rate (V_{max}) is a vegetation parameter that directly affects the photosynthesis rate (Zhan et al., 2003). The model simulated photosynthesis rates are controlled by three limitation factors related to Rubisco, electron transportation, and product sink. The vegetation parameter, V_{max}, plays a key role in this computation. It determines the photosynthetic limitations and serves as a link between the water and carbon cycles since it can also affect soil moisture through transpiration.

We have conducted a large number of experiments to test the parameters that affect the water and carbon cycle simulations in SSiB4/TRIFFID/SIF, and confirmed the importance of these four parameters mentioned above. The effects of the four parameters on soil moisture and SIF were tested through adjusting them within their normal ranges. Figure 2 shows the

194 schematic flowchart of the SSiB4/TRIFFID/SIF model. The black boxes are the model
195 components. The blue boxes are the satellite products used to evaluate the soil moisture and SIF
196 simulations and to calibrate the parameters. The brown box and the green boxes represent the
197 soil property parameters and the vegetation parameters tested and calibrated in this study,
198 respectively.

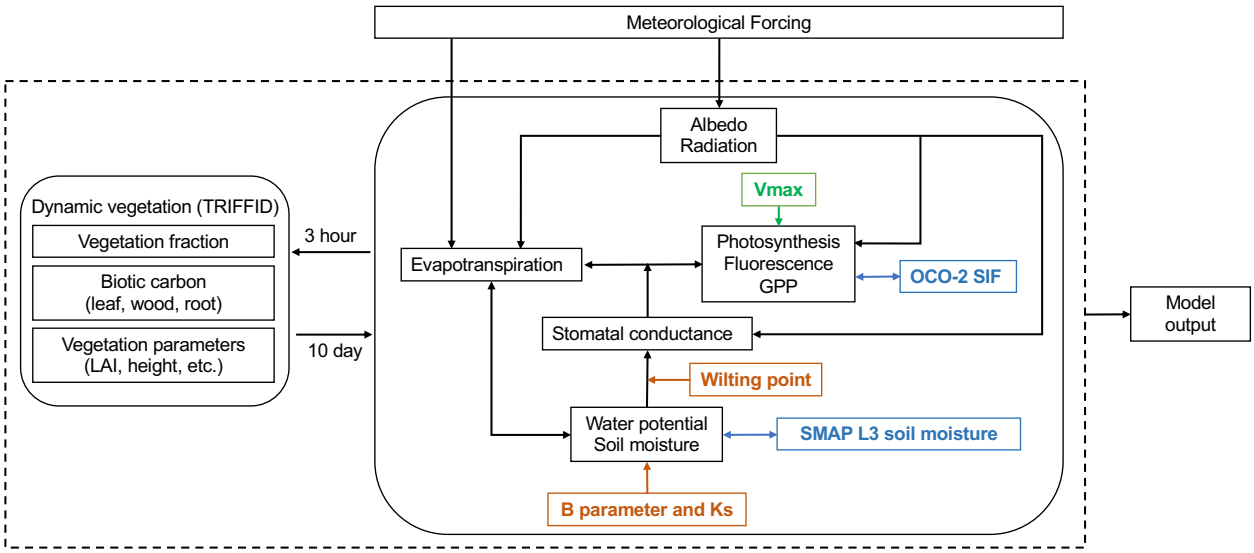

199

200 **Figure 2.** Overview flowchart of the SSiB4/TRIFFID/SIF model and the modified parameters in
201 the model. The black boxes are the SSiB4/TRIFFID/SIF model components; the brown boxes
202 represent the modified soil property parameters in the model; the green box represents the
203 modified vegetation parameters in the model; and the blue boxes are the satellite data. SMAP

L3: Soil Moisture Active Passive enhanced Level 3; OCO-2: Orbiting Carbon Observatory 2; LAI: leaf area index.

We designed the following four sets of experiments to assess the effects of the four critical parameters on soil moisture and SIF simulation with the dynamic vegetation model coupled and for further calibration in SSiB4/TRIFFID/SIF (Table 1).

1. For the control run (CTL), the original values of the parameters were used.
2. For Test 1, the B parameter was modified. Our preliminary experiments suggested this parameter has a larger impact on soil moisture than other parameters.
3. For Test 2, the calibrated B parameter based on Test 1 was used, and the K_s was tested.
4. For Test 3, the wilting point was tested with the calibrated B parameter and K_s based on Test 2.
5. For Test 4, the V_{max} was tested with the calibrated B parameter, K_s, and wilting point based on Test 3.

Table 1. SSiB4/TRIFFID/SIF Experiment Design.

	Experiment description
CTL	Original parameters
Test 1	With modified B parameter
Test 2	Same as Test 1 but with hydraulic conductivity at saturation (K_s) modified
Test 3	Same as Test 2 but with wilting point (Wp) modified
Test 4	Same as Test 3 but with maximum RuBP carboxylation rate (V_{max}) modified

2.3 Data

The SSiB vegetation map and table based on ground survey and satellite-derived information are used as the initial condition for SSiB2/SIF simulation and SSiB4/TRIFFID/SIF quasi-equilibrium simulation (Dorman & Sellers, 1989; Xe et al., 1996, Zhang et al., 2015). Meteorological forcing data are used to drive the model. The observation-based soil moisture, SIF, and GPP products are used to evaluate the model simulation and calibrate the model

parameterization. The regions at latitudes higher than 60°N were excluded from the analysis because of the scarce satellite records.

2.3.1 Meteorological forcing data

The three-hourly meteorological forcing data from 1948 to 2008 used for the quasi-equilibrium simulation in SSiB4/TRIFFID/SIF are from the Princeton global meteorological dataset for land surface modeling (Sheffield et al., 2006). The dataset combines global observation-based datasets with the NCEP/NCAR reanalysis. The spatial resolution is 1°×1°, and the temporal interval is 3 h. Its 60-year mean climatology with 3-h intervals was generated and interpolated bilinearly to 0.5°×0.5° to drive the quasi-equilibrium simulation. The hourly meteorological forcing data used for simulations in SSiB2/SIF and SSiB4/TRIFFID/SIF are the bias-corrected reconstruction of near-surface meteorological variables derived from the fifth generation of the European Centre for Medium-Range Weather Forecasts (ECMRF) atmospheric reanalysis (ERA5) (Cucchi et al., 2022). This dataset has 0.5°×0.5° spatial resolution and a 1-h temporal interval. The 3-hour average was generated to drive the transient simulations. The variables included in the meteorological forcings are surface air temperature (K), pressure (Pa), specific humidity (g kg^{-1}), wind speed (m s^{-1}), downward shortwave radiation flux (W m^{-2}), downward longwave radiation flux (W m^{-2}), and precipitation (kg m^{-2} s^{-1}).

2.3.2 Observation-based data

There is no human activity included in the SSiB4 model simulation. Therefore, the potential vegetation distributions produced by the quasi-equilibrium run in SSiB4/TRIFFID/SIF are not the same as the vegetation map observed by satellite-derived products over some areas due to anthropogenic effects, such as the croplands in the Central US, Southern Brazil, Europe, India, and Eastern China. In this study, we used the Global Land Cover (GLC) database for the year 2000 (Bartholome and Belward, 2005) derived from Satellite Pour 1'Observation de la Terre (SPOT) to exclude the cultivated and managed areas in simulation, evaluation, and analysis.

The Soil Moisture Active Passive (SMAP) mission, launched by NASA on January 31, 2015, is the newest L-band satellite dedicated to providing global surface soil moisture

measurements. This study used the SMAP Enhanced L3 Radiometer Global Daily 9 km EASE-Grid Soil Moisture dataset (SMAP L3). This dataset presents the volumetric surface soil moisture (m^3/m^3) at 0–5 cm and is superior to other satellite soil moisture products, including the Soil Moisture and Ocean Salinity (SMOS) and the ESA Climate Change Initiative (ESA CCI) in terms of capturing temporal trends compared with in-situ observations from global dense and sparse networks (Ma et al., 2019). The assessment of the SMAP L3 product using the in-situ measurements from the core validation sites (CVSs) shows that the average unbiased root mean square error (ubRMSE) is lower than 0.04 m^3/m^3 (Colliander et al., 2017; O'Neill et al., 2020). Zhang et al. (2019) validated the SMAP L3 product using extensive ground measurements from sparse networks and found that the retrievals from the descending (6:00 AM) product and ascending (6:00 PM) product do not show significant differences. In this study, the average of the descending and ascending products was bilinearly interpolated to 0.5°×0.5° for evaluation and calibration.

The SIF simulation was evaluated using the Orbiting Carbon Observatory-2 (OCO-2) SIF product. This mission, launched on July 2, 2014, measures SIF from the infilling of the Fraunhofer lines at 1:36 p.m. local time with a repeat frequency of approximately 16 days. The retrieval precision of OCO-2 is considerably improved over other existing satellite SIF products, including the Greenhouse Gases Observing Satellite (GOSAT) product and the Global Ozone Monitoring Experiment-2 product (GOME-2) (Sun et al., 2018). All soundings within a 1°×1° pixel were averaged and archived onto a 0.5° grid to generate OCO-2 SIF at 757 nm so that most of the pixels have sufficient soundings to retrieve the gridded monthly SIF (Qiu et al., 2020). To use this dataset to assess the model simulated SIF, the simulation at noon and 3 p.m. in each time zone was selected to obtain the one at 1 p.m. through interpolation.

Previous studies found that GPP and SIF had a strong linear relationship, and the satellite SIF data provide useful information on terrestrial GPP (Bacour et al., 2019; Joiner et al., 2013; Lee et al., 2015; Walther et al., 2016). Li et al. (2018) explored the relationship between OCO-2 SIF and tower GPP at 64 flux sites across the globe encompassing eight major biomes, confirming the strong correlation between SIF and GPP. Because of the significant uncertainty in the quantification of global GPP due to the lack of direct GPP observations at a global scale (Wang et al., 2021; Zhang and Ye, 2021), we selected three global GPP datasets derived from

observation using different methods for comparison rather than evaluation or calibration. First is the GLASS (Global Land Surface Satellite) GPP product generated from the Eddy Covariance – Light Use Efficiency (EC-LUE) model (Yuan et al., 2007). The EC-LUE model has been validated widely throughout various ecosystems using the measurements from eddy covariance towers (Li et al., 2013; Yuan et al., 2014), and Jia et al. (2018) indicated that the EC-LUE model performed better than the MODIS algorithms. This dataset has 0.05°×0.05° horizontal resolution and 8-day time intervals. The second GPP product used for comparison is the FLUXCOM RS GPP product. It uses machine learning to merge the carbon flux measurements from the FLUXNET eddy covariance towers and remote sensing data (Tramontana et al., 2016). Zhang and Ye (2021) evaluated 45 global terrestrial GPP products by taking Model Ensemble GPP derived from observations as the reference dataset and recommended the RS product for global GPP comparison. Its resolution is 0.5°×0.5° and the time interval is 8 days. The last dataset is a global MODIS and FLUXNET-derived GPP product (FLUXSAT GPP) (Joiner and Yoshida, 2021). It used MODIS product as input to neutral networks to globally upscale GPP estimates from selected FLUXNET eddy covariance tower sites (Joiner and Yoshida, 2020). The product has a 0.05° spatial resolution and a daily temporal resolution.

3 Results

3.1 Assessment of the simulated vegetation distribution

The rate of change in vegetation fraction is less than 2% over the last 10 years of simulation, which means it reached a steady state after a 100-year spin-up (Liu et al., 2019) (Figure S1). For most PFTs, the rate is less than 1.5%. Using initial vegetation conditions derived from this quasi-equilibrium state, SSiB4/TRIFFID/SIF was driven with the historical meteorological forcing and yearly updated atmospheric CO_2 concentration from 1979 to 2019. The simulated vegetation spatial distribution was compared with that simulated in the previous study (Liu et al., 2019) to ensure that the simulated vegetation spatial distribution is reasonable, which is the base for other simulated variables in the model. The evergreen broadleaf trees in the Amazon, central Africa, and Indonesia, needleleaf trees in midlatitudes and high latitudes of North America and Eurasia, deciduous broadleaf trees in southeastern US, C_3 grasses in central

US, South America, Eurasian Steppe, Africa, and east Australia, C_4 plants in southeast US, South America, Africa, Southeast Asia, and northern Australia, and shrubs in the semi-arid areas are reasonably simulated (Figure S2). Overall, the simulated vegetated area covers 77.5% of the global land surface. The simulated tree, C_3 grass, C_4 plants, and shrubs cover 31.1%, 11.3%, 15.3%, and 14.5%, respectively. These fractions are consistent with those in the study of Liu et al. (2019).

3.2 Effects of dynamic vegetation processes on SM, SIF, and GPP simulations

The spatial distribution of the global SIF simulated by SSiB2/SIF and SSiB4/TRIFFID/SIF were evaluated against the OCO-2 measurements in Figure 3. The SIF simulated in SSiB2/SIF shows a negative bias in the South American and African savanna regions, southeast China, and east US, while a positive bias in the boreal forest in North America and North and Central Asia. In SSiB4/TRIFFID/SIF, the simulated SIF bias is positive in most regions, especially in semi-arid regions such as the Western United States, southwest South America, Africa, Central Asia, and Australia. Its positive bias is smaller in boreal forests compared with that in SSiB2/SIF. Table 2 lists the global spatial correlation coefficient (SCC), bias (BIAS), and root-mean-square error (RMSE) of the simulated SIF in SSiB2/SIF and SSiB4/TRIFFID/SIF compared with the OCO-2 SIF data. The SCC increased by 10%, and the RMSE decreased by 12% in SSiB4/TRFFID/SIF, which shows an improvement in the spatial pattern of the simulated SIF in the run with dynamic vegetation included. However, the absolute value of the global mean SIF bias increased in SSiB4/TRIFFID/SIF. The improvement in SCC indicates that the vegetation spatial distribution simulated by SSiB4/TRIFFID/SIF is more realistic than the observation-based one used in SSiB2/SIF and further confirms the reasonability of the vegetation distribution simulation. The simulated SIF in different seasons was also compared with OCO-2 SIF data. The highest RMSE of simulation compared to OCO-2 occurs in summer both in SSiB2/SIF and SSiB4/TRIFFID/SIF. The most obvious improvement in

337 SSiB4/TRIFFID/SIF appears in spring, with the SCC increasing by 37% and the RMSE
338 decreasing by 18%.

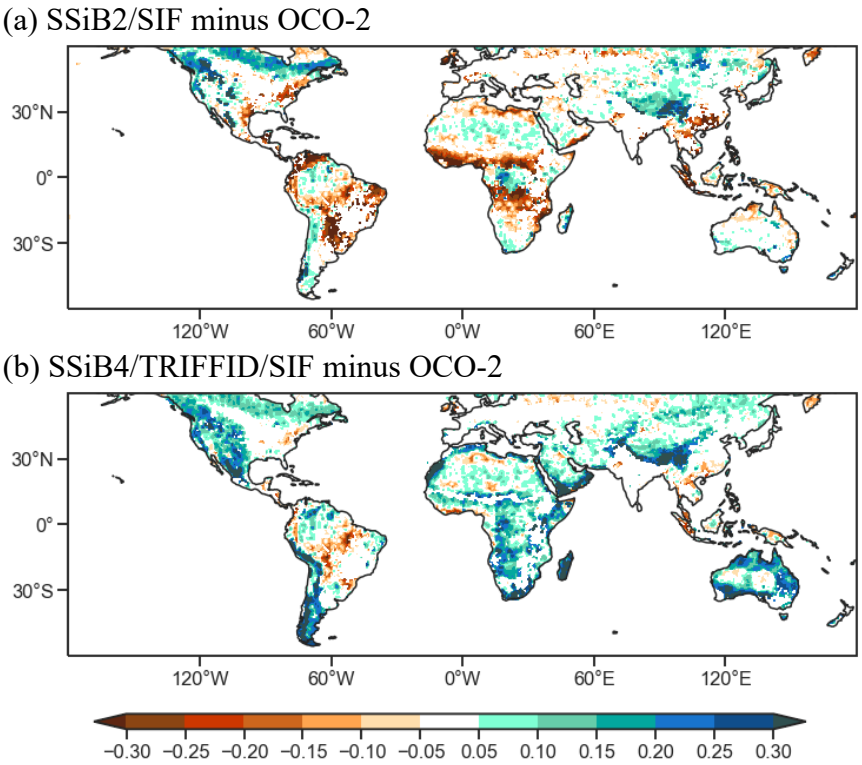

339

340 **Figure 3.** Global differences of solar-induced chlorophyll fluorescence (SIF) between
341 simulations in (a) SSiB2/SIF, (b) SSiB4/TRIFFID/SIF and Orbiting Carbon Observatory 2
342 (OCO-2) data. Units: W/m^2/μm/sr.

343

344 **Table 2.** Spatial Correlation Coefficient (SCC), Mean Bias (BIAS), and Root-Mean-Square
345 Error (RMSE) of annual SIF simulations compared to OCO-2 data. Units: W/m^2/μm/sr.

	SSiB2/SIF	SSiB4/TRIFFID/SIF
SCC	0.779	0.864
BIAS	-0.043	0.064
RMSE	0.169	0.143

346

347 The GPP simulation in SSiB2/SIF and SSiB4/TRIFFID/SIF was compared with
348 observation-based estimated GPP in 2015, excluding the polar regions. In the three observation-
349 based estimates, the global GPP ranges from 835.2 to 1088 g C/m^2/yr, with a median of 867.3 g
350 C/m^2/yr. Figure 4 shows that the global GPP simulated by SSiB2/SIF is much lower than the
351 observation-based estimations, with a value of 533.2 g C/m^2/yr. The simulated global GPP in
352 SSiB4/TRIFFID/SIF is 875.2 g C/m^2/yr, which is close to the median value of the three
353 observation-based estimates. Figure 5 further compared the latitudinal distribution of zonal
354 mean GPP among the observation-based estimates and model simulations. The GLASS and
355 FLUXSAT products demonstrate higher GPP values near the equator, while the FLUXCOM
356 product has higher GPP values in subtropical regions in the Northern Hemisphere. The
357 SSiB2/SIF GPP simulation is lower than the observation-based GPP products at all latitudes.
358 The SSiB4/TRIFFID/SIF GPP simulation is close to the observation-based estimates except near
359 the tropics, where the observation-based estimates show large discrepancies. Therefore, the
360 SSiB4/TRIFFID/SIF simulation is within the range of various observations. Introducing the
361 dynamic vegetation process can lead to significant improvement in GPP simulation throughout
362 the globe. The plausible reason that may contribute to the improvement of GPP simulation in
363 SSiB4/TRIFFID/SIF is the diversity of PFTs existing in a single grid box. In SSiB2/SIF, there is
364 only one PFT in one grid box with the vegetation parameters, such as vegetation fraction cover
365 (FRAC), LAI, and vegetation height (VH), specified based on a vegetation table (Sellers et al.,
366 1996). In SSiB4/TRIFFID/SIF, each grid box consists of 7 PFTs, with the competition among
367 them. The vegetation parameters are updated based on the carbon budget and related to the
368 surface energy and water cycles. The improvement shows that the dynamic vegetation process

369 can substantially improve the simulation of the carbon process and can help to provide a
370 reasonable simulation of vegetation conditions and carbon fluxes.

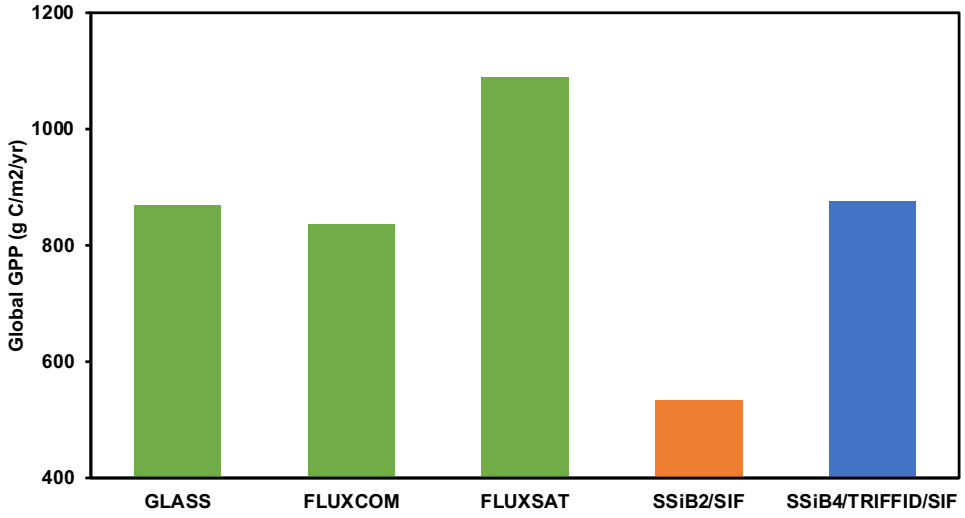

371

372 **Figure 4.** Comparison among observation-based estimated, SSiB2/SIF simulated, and
373 SSiB4/TRIFFID/SIF simulated global GPP in 2015 (60°S–75°N). Units: g C/m^2/yr.

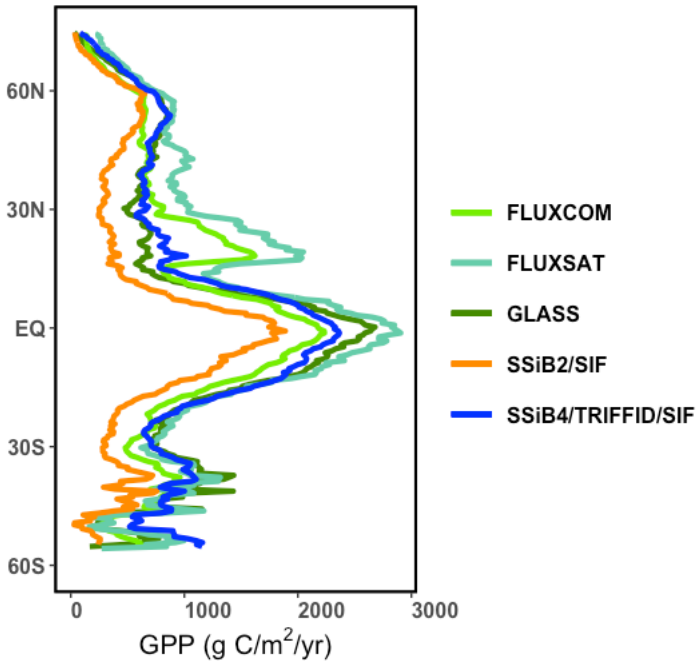

374

Figure 5. Comparisons of the latitudinal distribution of the zonal mean GPP among the observation-based estimates, SSiB2/SIF simulation, and SSiB4/TRIFFID/SIF simulation. Units: g C/m^2/yr.

Figure S3 compares the simulated soil moisture in SSiB2/SIF and SSiB4/TRIFFID/SIF with SMAP L3 soil moisture data. Over the globe, there was only marginal improvement in SSiB4/TRIFFID/SIF compared with SSiB2/SIF (Table S1). However, in SSiB4/TRIFFID/SIF, the global simulated SIF is higher, which represents higher photosynthesis and transpiration, the simulated soil evaporation rate is much lower, leading to a marginal change in simulated evapotranspiration. The spatial patterns of the soil moisture bias in SSiB2/SIF and SSiB4/TRIFFID/SIF are similar. The models underestimated the surface soil moisture in most areas, such as the North American boreal forest, Eastern United States, Amazon Basin, equatorial Africa, and Southeast Asia. The soil moisture was overestimated in the Eurasian boreal forest and central Asia. Calibration of the parameters directly related to soil property and affecting the vertical soil water distribution in SSiB4/TRIFFID/SIF is needed to improve the soil moisture simulation, which will be discussed in Section 3.4.

3.3 SIF−soil moisture relationship

Soil moisture plays a dominant role in determining dryness stress on ecosystem production over most vegetated areas (Liu et al., 2020). Several studies have analyzed the influence of soil water content limitation on vegetation productivity using various satellite products. Short Gianotti et al. (2019) found that the SIF−soil moisture relationship has increasing response strength with aridity, with little in the light-limited humid regions of the contiguous United States. Jonard et al. (2022) distinguished the water-limited and light-limited environments using the TROPOspheric Monitoring Instrument (TROPOMI) SIF data and the SMAP multitemporal dual channel algorithm (MT-DCA) soil moisture data in the growing season. We calculated the Pearson correlation coefficient between model-simulated SIF and soil moisture and evaluated it against that between OCO-2 SIF and SMAP L3 soil moisture. The SIF and soil moisture data used here are monthly data with seasonal cycles removed. Figure 6 shows the comparison of the correlation coefficient distribution between soil moisture and SIF in observation and simulation. The observed SIF−soil moisture correlation map shows a significant

positive correlation over most regions, suggesting the water limitation on vegetation growth. Both SSiB2/SIF and SSiB4/TRIFFID/SIF simulations show a strong correlation between soil moisture and SIF anomalies in semi-arid regions, such as the Western United States, South American savanna, and South and East Africa. Meanwhile, both SSiB2/SIF and SSiB4/TRIFFID/SIF produce negative correlations over the Eastern United States, La Plata Basin, and south China, which is opposite to that in the observation. Over the Eurasian Steppe and coastal Australia, SSiB2/SIF and SSiB4/TRIFFID/SIF simulations show different correlation relationships. The SSiB4/TRIFFID/SIF model produced a positive relationship consistent with that derived from satellite data, while in SSiB2/SIF, the relationship is negative. The SIF−soil moisture correlation derived from the simulations in SSiB4/TRIFFID/SIF is more consistent with that derived from satellite data, showing that the coupling with the dynamic vegetation model

helps to better capture the effects of monthly soil moisture dynamics on vegetation photosynthetic activities.

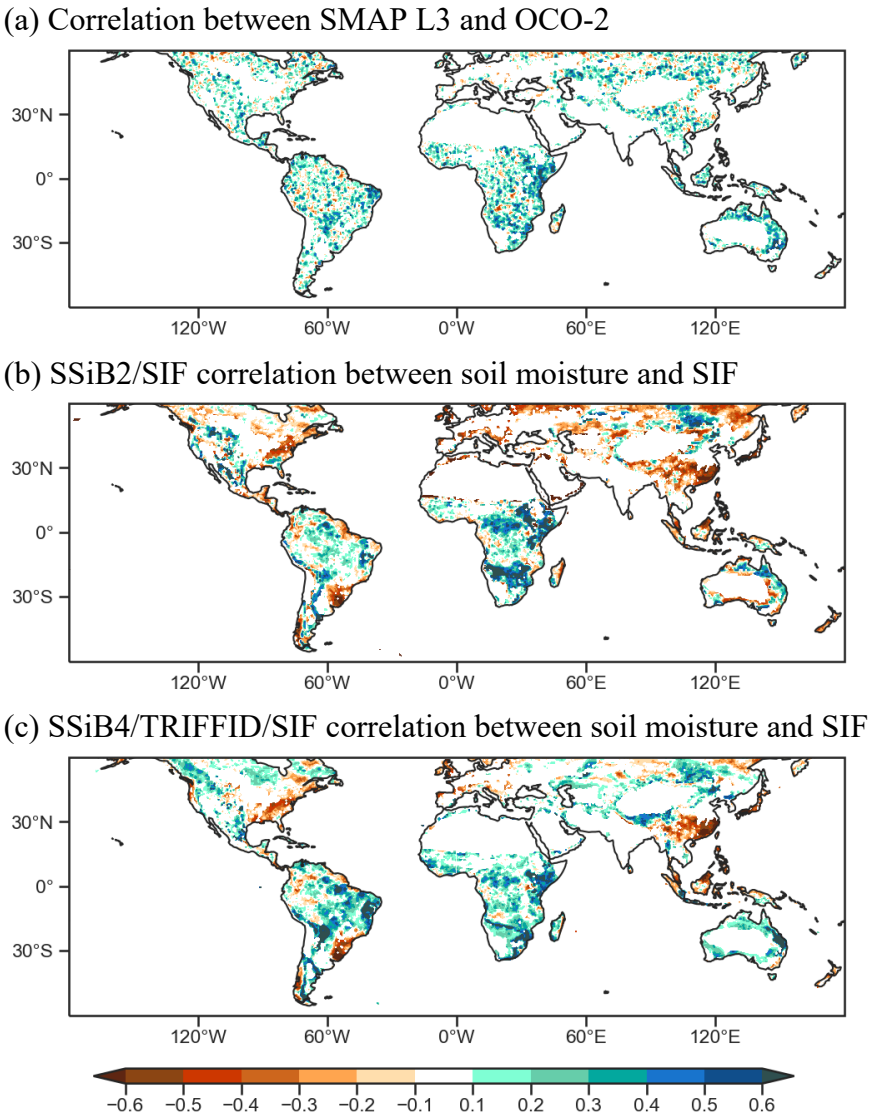

Figure 6. Comparisons of the correlations in the Northern Hemisphere summer between the monthly anomalies of (a) SMAP L3 soil moisture data and OCO-2 SIF data, (b) the SSiB2/SIF

simulated soil moisture and SIF, and (c) the SSiB4/TRIFFID/SIF simulated soil moisture and SIF.

3.4 Effects of key parameters on soil moisture and SIF simulation

The B parameter, K_s, wilting point, and V_{max} were changed within the normal range of soil and vegetation property variations to conduct experiments to show the model sensitivity to changes in the parameters (Beerling and Quick, 1995; Von Caemmerer and Furbank, 1999; Xue et al., 1996) (Table 3). The experiments covered the period from 2010 to 2019. The years from 2010 to 2014 were used for spin-up, and the annual results from 2015 to 2019 were analyzed.

Table 3. Soil and vegetation parameters used in the sensitivity experiments.

	Values
B parameter	3, 4, 5, 6, 7, 8, 9
K_s	2E-3, 2E-4, 2E-5, 2E-6, 2E-7
Wilting point	2, 4, 6, 8, 10, 12
V_{max}	20, 40, 60, 80, 100, 120, 140 (μmol/m^2/s)

3.4.1 Soil property parameters

Previous studies have shown that the soil property parameters are one of the key sources of uncertainties in soil moisture simulation in land surface models (Demaria et al., 2007; Qiu et al., 2018). According to previous work, carbon fluxes are also sensitive to soil parameters in the SSiB model (Prihodko et al., 2008). To improve the soil moisture and SIF simulation in SSiB4/TRIFFID/SIF and to better understand the role of the parameters determining the soil texture in the interactions between the water and carbon cycles, we examined the effects of B

parameter, K_s, and wilting point on soil moisture and SIF simulation in SSiB4/TRIFFID/SIF (Figure 7).

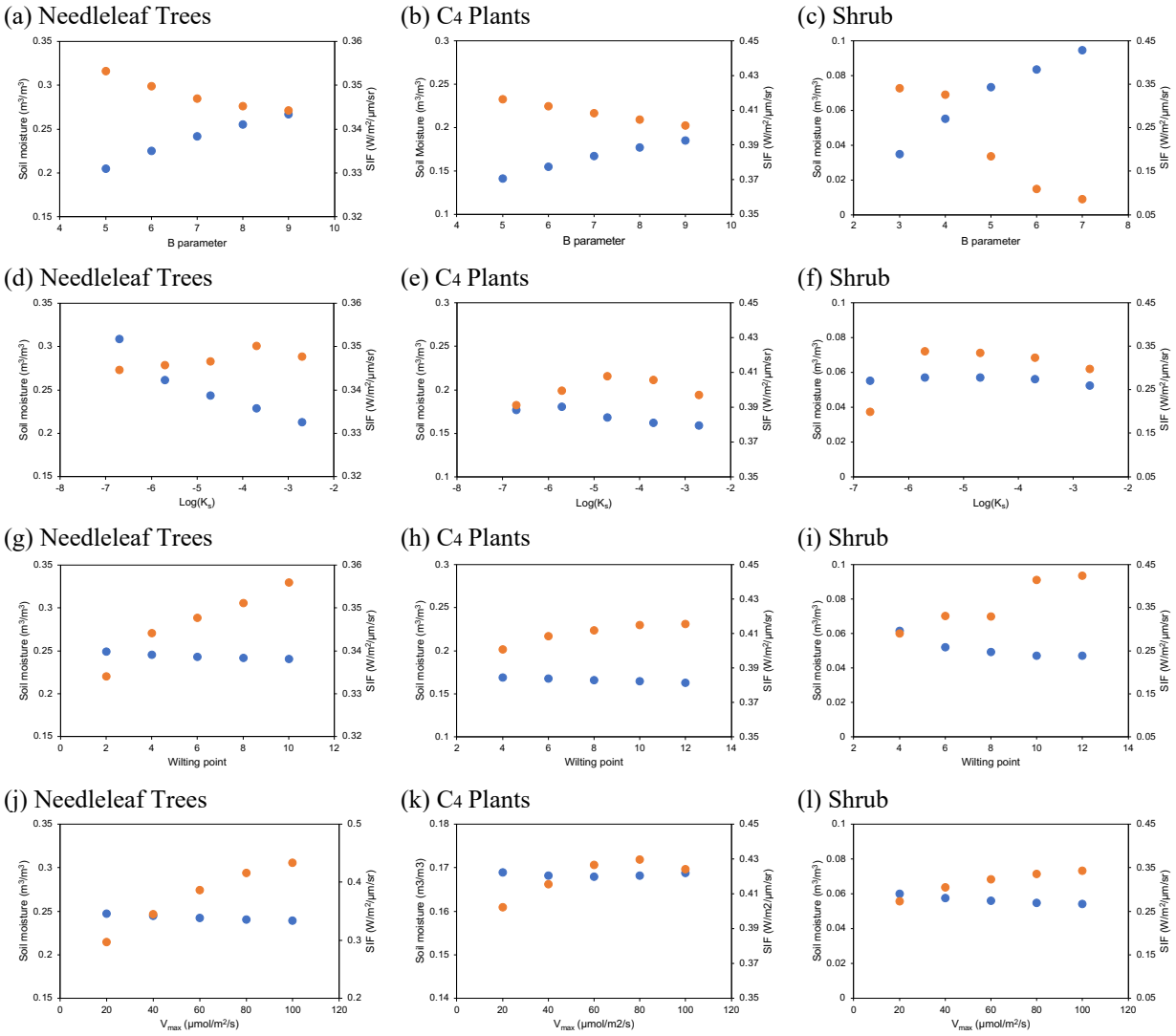

Figure 7. Calculated soil moisture (blue), SIF (orange) for (a, d, g, j) needleleaf trees, (b, e, h, k) C_4 plants, and (c, f, i, l) shrubs under different (a, b, c) B parameter; (d, e, f) logarithm of K_s; (g, h, i) wilting point, and (j, k, l) V_{max}.

The effects of the B parameter on water and carbon cycles are complex. With a higher B parameter, soil moisture increased, and SIF decreased (Figures 7a, 7b, 7c). A higher B

parameter represents a soil texture closer to clay, which leads to more difficulty in soil evaporation and more soil moisture. Meanwhile, soil hydraulic conductivity decreased with increased B parameter (Eq. 2), which reduced the total runoff and may have increased evaporation; however, the change in evaporation was marginal. Overall, a higher B parameter is associated with more soil moisture. Moreover, the B parameter indirectly modifies SIF through its effect on the wilting point. The change in the B parameter modifies the relationship between soil water potential and soil water content through the retention curve. When the B parameter is higher, for a given amount of soil water content, the absolute value of water potential increases, and then the β factor in Eq. 3 is reduced, leading to stomata close and lower SIF and transpiration. In the tropics, the soil moisture increased with a larger B parameter while the SIF and transpiration almost stayed the same. The abundant soil water content in the rainforests keeps the β factor high in the change of the B parameter.

As for K_s, the soil moisture decreases when K_s is higher (Figures 7d, 7e, 7f). Higher K_s indicates that the soil texture is closer to sand, increasing surface infiltration and changing the vertical soil water content distribution. The hydraulic conductivity is larger with higher K_s, leading to larger drainage and decreased total soil water content. When K_s becomes very low, the surface infiltration becomes extremely low, leading to much larger runoff and low root zone soil moisture. The low root zone soil water potential under low K_s conditions in SSiB4/TRIFFID/SIF lead to lower β factor and SIF. Therefore, the SIF drops in SSiB4/TRIFFID/SIF when the K_s value is very small. In humid regions, it is hard for the soil water content to drop to a value at which photosynthesis weakens, so the SIF does not change obviously (Figure 7d).

For the wilting point, when it increases, the soil moisture, at which the stomata close completely, drops, leading to a higher β factor (Eq. 3), allowing more open stomata and higher stomatal conductance, which leads to higher SIF and photosynthesis and transpiration rates (Figures 7g, 7h, 7i). For example, in South Africa covered by savanna, when the wilting point increased from 4 to 10, the corresponding volumetric soil moisture at which β factor started to increase rapidly decreased from 0.30 to 0.13 m^3/m^3, and the simulated SIF increased from 0.40 to 0.42 $W/m^2/\mu m/sr$ (Figure 7h). Since a higher wilting point leads to higher transpiration rates, the soil moisture decreases with the increase of the wilting point. However, the effects of the

wilting point on soil moisture are not as efficient as that of the B parameter and K_s. For example, the soil moisture in South Africa dropped slightly from 0.169 to 0.165 m^3/m^3 when the wilting point increased from 4 to 10 (Figure 7h).

3.4.2 Vegetation parameter

Photosynthesis is an important process of the terrestrial carbon cycle, and it is simulated in SSiB2/SIF and SSiB4/TRIFFID/SIF following the analytical solution approach developed by Zhan et al. (2003) based on the Collatz et al. (1991) and Collatz et al. (1992) model. The vegetation parameter directly related to photosynthesis, V_{max}, varies considerably among and within plant functional types (PFTs) (Kattge et al., 2009; Wang et al., 2021; Wullschleger, 1993), and it cannot be measured directly but must be inferred by model inversion from photosynthesis measurements. The terrestrial biosphere models demonstrate considerable sensitivity in carbon flux simulation given the uncertainty in V_{max} (Bonan et al., 2011; Piao et al., 2013). To further improve the carbon flux simulation in SSiB4/TRIFFID/SIF and to explore the effects of this vegetation parameter on water and carbon cycles, we examined the effects of V_{max} on soil moisture and SIF simulation in SSiB4/TRIFFID/SIF.

As demonstrated in Figure 7j, the photosynthesis rates of needleleaf trees are especially sensitive to the change in V_{max} in all the PFTs simulated in SSiB4/TRIFFID/SIF. When the V_{max} value increased from 20 to 100 $\mu mol/m^2/s$, the SIF simulation increased dramatically from 0.30 to 0.43 $W/m^2/\mu m/sr$, which is a much more marked increment compared with the changes in the B parameter, K_s, and wilting point as shown in Section 3.4.1. For other PFTs, the effects of V_{max} on SIF simulation are also significant. For example, with the V_{max} changing from 20 to 80 $\mu mol/m^2/s$, the SIF simulation increased from 0.40 to 0.43 $W/m^2/\mu m/sr$ in the South African savanna, and the SIF simulation increased from 0.27 to 0.34 $W/m^2/\mu m/sr$ in shrubland in the Western United States (Figure 7k). The effects of V_{max} on soil moisture simulation are similar to that of the wilting point. With the increasing V_{max}, the photosynthesis rates are higher, leading to higher SIF and transpiration rates, which results in lower soil moisture. For example, in the

503 Western United States, the soil moisture decreased from 0.060 to 0.054 m^3/m^3 when the V_{max}
504 increased from 20 to 100 μmol/m^2/s (Figure 7l).

505 3.5 Improvement in soil moisture and SIF simulation after calibration

506 Based on the tests in section 3.4, we identified that the B parameter, K_s, wilting point,
507 and V_{max} are the key parameters that significantly impact both soil moisture and SIF simulations
508 in SSiB4/TRIFFID/SIF. To identify their impact on soil moisture and SIF simulation, we first
509 conducted a set of experiments with individual parameters modified in each test. The B
510 parameter, K_s, wilting point, and V_{max} were modified in Test B, Test K_s, Test Wp, and Test V_m.
511 The range of these parameters is according to the sensitivity tests in section 3.4. The soil
512 moisture and SIF in the control run and the four tests were calculated and compared with the
513 SMAP L3 and OCO-2 data at global scales. In the tests with the modified soil parameters, the
514 parameter set with minimum RMSE in soil moisture is identified as the optimized set, and the
515 experiment with this set of parameters will be referred to as Test B opt, Test K_s opt, and Test Wp
516 opt, while in the test with the modified vegetation parameter, the parameter set with minimum
517 RMSE in SIF is identified as the optimized set, Test V_m opt.

518 Figure 8 shows the improvement in the global mean bias and RMSE of soil moisture and
519 SIF simulations in each test with the optimized values relative to SMAP L3 soil moisture and
520 OCO-2 SIF data. The most significant improvement in soil moisture and SIF simulations both
521 occurred in Test B, and the most significant improvement in SIF simulation happened in Test
522 V_m. The improvement in soil moisture simulation is also substantial in Test K_s, but the effects of
523 K_s are less efficient than the B parameter. Through this set of tests, we found that the
524 improvement of both soil moisture and SIF simulation is most with the change in the B
525 parameter. The soil moisture simulation is most sensitive to the B parameter and K_s, while the
526 SIF simulation is most sensitive to V_{max}. Based on these results, we designed another set of
527 experiments listed in Table 1 to get optimal values of the four parameters in
528 SSiB4/TRIFFID/SIF. The tests with the set of optimal parameters will be referred to as Test 1
529 opt, Test 2 opt, Test 3 opt, and Test 4 opt. The soil moisture and SIF in the control run and four
530 tests were evaluated at global scales and for the six PFTs, including the Evergreen Broadleaf

531 Trees (EBT), Needleleaf Trees (NT), C_3 Grasses (C_3), C_4 Plants (C_4), Shrub (SH), and
532 Deciduous Broadleaf Trees (DBT).

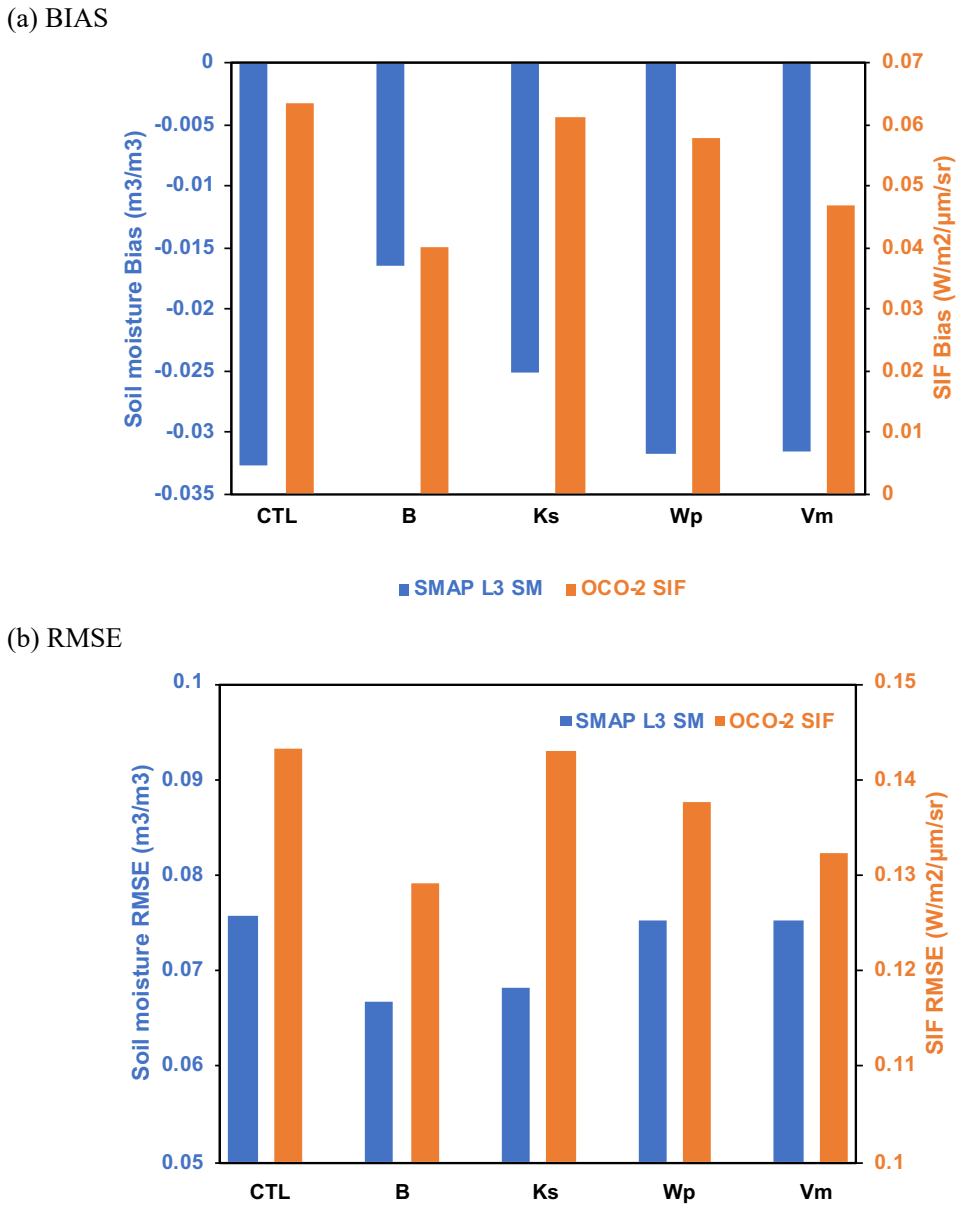

533

534 **Figure 8.** Global (a) mean bias (BIAS) and (b) root-mean-square error (RMSE) in the control
535 run (CTL), Test B opt (B), Test K_s opt (Ks), Test Wp opt (Wp), and Test V_{max} opt (Vm) relative
536 to SMAP L3 soil moisture and OCO-2 SIF data.

537

Figure 9 shows the global mean bias and RMSE of soil moisture and SIF relative to SMAP L3 soil moisture and OCO-2 SIF data in the control run, Test 1 opt, Test 2 opt, Test 3 opt, and Test 4 opt. The optimal B parameter led to significant improvement in both soil moisture and SIF, with the global mean bias decreasing by 49.6% (from -0.033 to -0.0165 m^3/m^3) and by 37.0% (from 0.064 to 0.040 $W/m^2/\mu m/sr$), respectively, and with the RMSE decreasing by 11.9% (from 0.076 to 0.067 m^3/m^3) and by 9.9% (from 0.143 to 0.129 $W/m^2/\mu m/sr$), respectively. The optimal K_s also improved both soil moisture and SIF simulation but with reduced magnitude in SIF. The global mean bias decreased by 22.7% and 13.7%, respectively, and the global RMSE decreased by 4.6% and 0.3%, respectively. Wilting point calibration also improved the simulation but with less magnitude in soil moisture. It decreased the mean bias by 5.8% and 11.2%, respectively, and the RMSE by 0.3% and 3.1%, respectively. The calibrated V_{max} further improved the SIF simulation substantially by 44.0% on the global mean bias and

550 5.9% on the RMSE and improved the soil moisture simulation slightly by 14.6% on the global
551 mean bias.

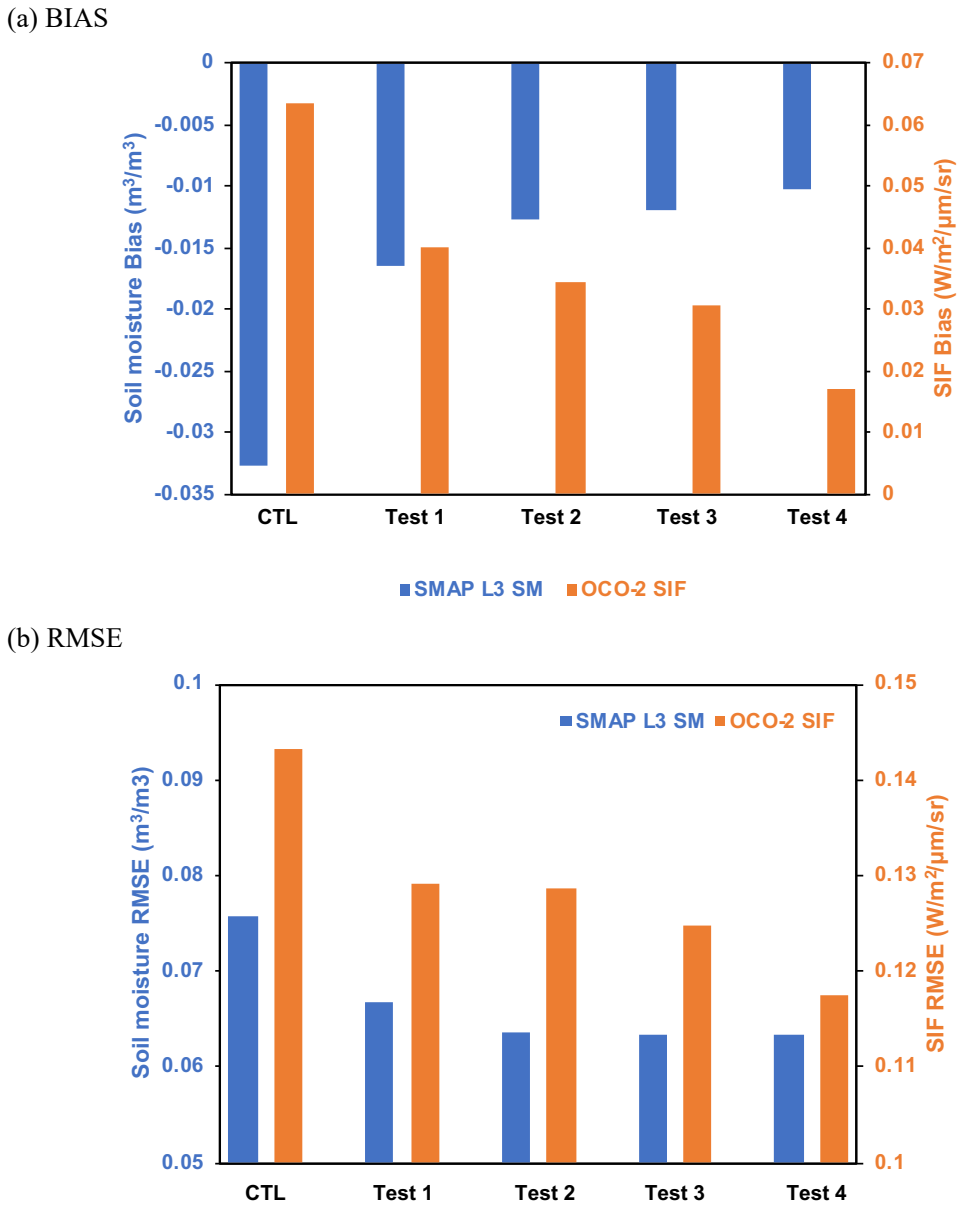

552

553 **Figure 9.** Global (a) mean bias (BIAS) and (b) root-mean-square error (RMSE) in the control
554 run (CTL), Test 1 opt, Test 2 opt, Test 3 opt, and Test 4 opt relative to SMAP L3 soil moisture
555 and OCO-2 SIF data.

556

Figures 10a and 10b illustrate the spatial distribution of global differences between simulated and SMAP L3 soil moisture and between simulated and OCO-2 SIF. The SSiB4/TRIFFID/SIF model significantly underestimated the soil moisture in most regions, especially in the tropics and semi-arid regions, while overestimating the SIF throughout the globe, with the most significant overestimation occurring in the semi-arid regions covered by shrubs and savanna. To delineate the spatial distribution of improvement in each test, Figures 10c to 10j show the soil moisture and SIF differences between simulations and observations in the test runs and the control run, and Table 4 lists the spatial correlation coefficient (SCC), mean bias (BIAS), and RMSE of the soil moisture and SIF at the global scale and for different vegetation types in the test runs and the control run. The most significant improvement for soil moisture simulation was in tropical rainforests and semi-arid regions. In Test 1 opt, with the B parameter modified, the soil moisture increased substantially over the tropics in the Amazon basin and Central Africa and in semi-arid regions, such as the Western United States, south Argentina, Sahel, South Africa, and Australia (Figure 10c). The soil moisture BIAS of EBT decreased from -0.103 to -0.069 m^3/m^3 and the RMSE from 0.124 to 0.097 m^3/m^3. The BIAS and RMSE of SH decreased from 0.057 to 0.043 m^3/m^3 and from 0.057 to 0.043 m^3/m^3, respectively, in soil moisture simulation. The SIF simulation was improved together with soil moisture in Test 1 in semi-arid regions covered by shrubs, including the Western United States, South Africa, and coastal Australia (Figure 10d). The BIAS and RMSE of SIF simulation for SH decreased from 0.130 to 0.018 $W/m^2/\mu m/sr$, and from 0.174 to 0.096 $W/m^2/\mu m/sr$. With the modification of K_s in Test 2 opt, the soil moisture simulation in the tropics was further improved (Figure 10e), with the BIAS and RMSE of EBT further decreased to -0.043 m^3/m^3 and 0.082 m^3/m^3, and both the soil moisture and SIF simulations were improved in the savanna in Africa, the Sahel, and coastal Australia (Figure 10e and Figure 10f). In Test 3 opt, the soil moisture simulation was slightly improved for C_3 and DBT, and the SIF simulation was improved for most PFTs, including EBT, C_3, C_4, SH, and DBT (Table 4). In Test 4 opt, the V_{max} modification significantly improved SIF simulation in the boreal forests in North America and Siberia and the grassland in the central United States and South America (Figure 10j). The BIAS and RMSE of NT in SIF simulation decreased from 0.080 to 0.036 $W/m^2/\mu m/sr$ and from 0.128 to 0.099

586 W/m^2/μm/sr. For C_3, the BIAS and RMSE of SIF simulation decreased from 0.111 to 0.081
587 W/m^2/μm/sr and from 0.174 to 0.153 W/m^2/μm/sr.

588

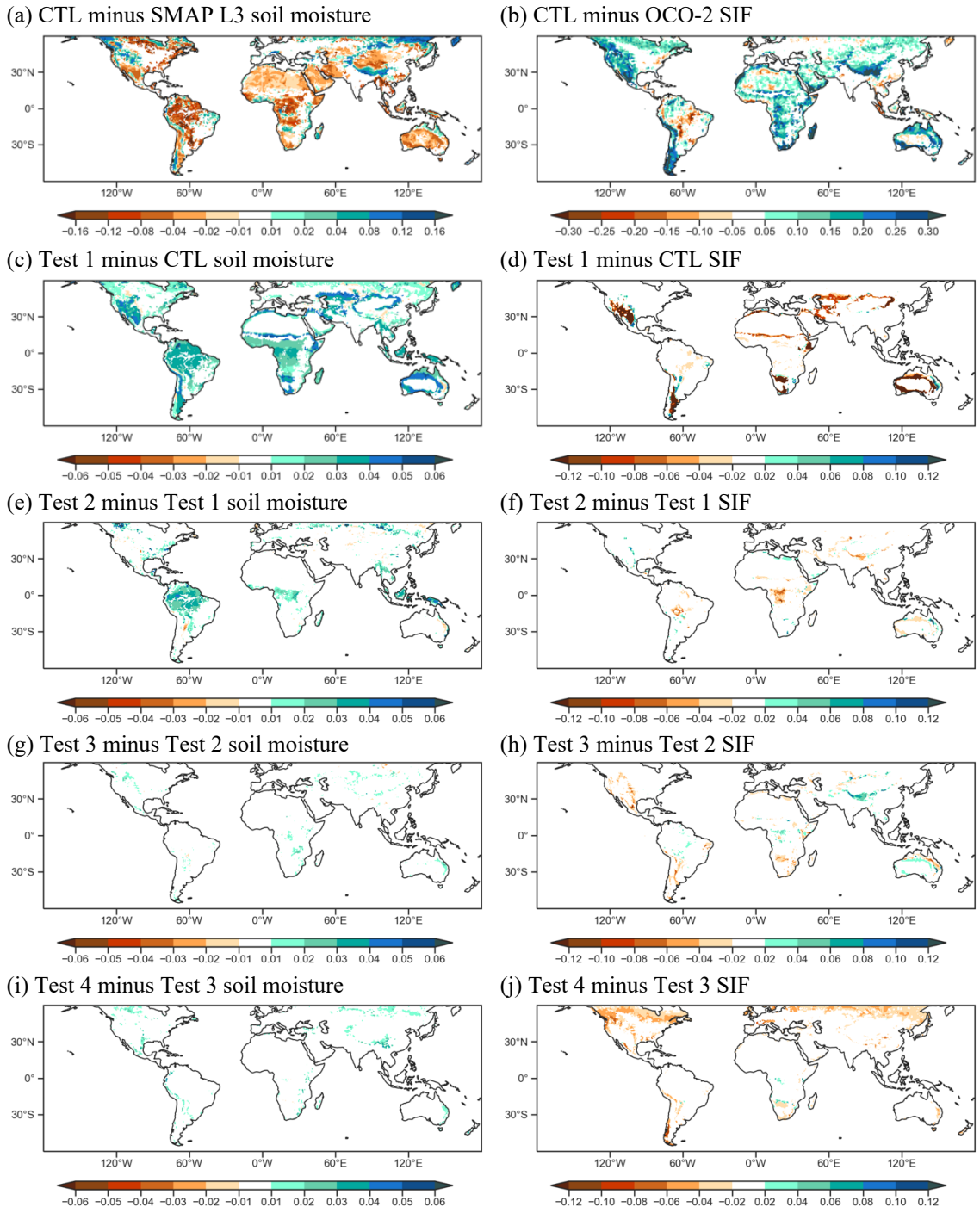

589

590 **Figure 10.** Global differences of simulated soil moisture and SIF in the control run compared to
591 (a) SMAP L3 (units: m^3/m^3) and (b) OCO-2 (units: $W/m^2/\mu m/sr$). Global differences of
592 simulated soil moisture (c, e, g, i) (units: m^3/m^3) and SIF (d, f, h, j) (units: $W/m^2/\mu m/sr$) in the
593 control run and different tests. (c, d) Test 1 opt minus CTL, (e, f) Test 2 opt minus Test 1 opt, (g,
594 h) Test 3 opt minus Test 2 opt, (i, j) Test 4 opt minus Test 3 opt.

595

596 **Table 4.** Spatial Correlation Coefficient (SCC), Mean Bias (BIAS), and Root-Mean-Square
597 Error (RMSE) of the comparison between SSiB4/TRIFFID/SIF simulated and observation-based
598 soil moisture and SIF. Units for soil moisture: m^3/m^3. Units for SIF: $W/m^2/\mu m/sr$.

Vegetation Type	Experiment	Soil Moisture			SIF		
		SCC	BIAS	RMSE	SCC	BIAS	RMSE
Evergreen Broadleaf Trees (EBT)	CTL	0.366	-0.103	0.124	0.150	-0.016	0.124
	Test 1 opt	0.366	-0.069	0.097	0.119	-0.023	0.128
	Test 2 opt	0.335	-0.043	0.082	0.120	-0.037	0.130
	Test 3 opt	0.332	-0.042	0.081	0.136	-0.035	0.128
	Test 4 opt	0.330	-0.042	0.081	0.141	-0.035	0.128
Needleleaf Trees (NT)	CTL	0.304	-0.012	0.087	0.411	0.082	0.130
	Test 1 opt	0.288	0.000	0.087	0.413	0.081	0.130
	Test 2 opt	0.302	0.003	0.086	0.402	0.078	0.128
	Test 3 opt	0.303	0.003	0.086	0.422	0.080	0.128
	Test 4 opt	0.312	0.006	0.086	0.439	0.036	0.099
C_3 Grasses (C_3)	CTL	0.489	0.012	0.070	0.407	0.124	0.187
	Test 1 opt	0.494	0.002	0.069	0.390	0.126	0.189
	Test 2 opt	0.498	-0.006	0.069	0.392	0.125	0.188
	Test 3 opt	0.498	-0.003	0.068	0.418	0.111	0.174
	Test 4 opt	0.508	0.008	0.069	0.406	0.081	0.153
C_4 Plants (C_4)	CTL	0.662	-0.042	0.080	0.491	0.055	0.151
	Test 1 opt	0.671	-0.022	0.071	0.514	0.044	0.145
	Test 2 opt	0.674	-0.017	0.069	0.518	0.036	0.142
	Test 3 opt	0.676	-0.016	0.069	0.542	0.026	0.138
	Test 4 opt	0.676	-0.014	0.069	0.550	0.020	0.136
Shrub (SH)	CTL	0.540	-0.034	0.057	0.368	0.130	0.174
	Test 1 opt	0.541	-0.000	0.043	0.612	0.018	0.096
	Test 2 opt	0.533	-0.001	0.043	0.617	0.008	0.098
	Test 3 opt	0.536	0.001	0.043	0.605	-0.001	0.091
	Test 4 opt	0.538	0.001	0.043	0.601	-0.005	0.090
Deciduous Broadleaf	CTL	0.858	-0.054	0.090	0.264	0.075	0.222
	Test 1 opt	0.861	-0.030	0.077	0.261	0.073	0.221

Trees (DBT)	Test 2 opt	0.864	-0.014	0.070	0.198	0.072	0.228
	Test 3 opt	0.866	-0.014	0.069	0.224	0.068	0.222
	Test 4 opt	0.864	-0.014	0.069	0.248	0.045	0.211

4 Discussion

This study shows that the B parameter is a key parameter that connects the water and carbon cycles in SSiB models and has significant effects on both soil moisture and SIF simulations. The B parameter has the largest impact on soil moisture for all PFTs, and its effect on SIF varies among different vegetation types. The impact on SIF simulation is larger over semi-arid regions where the soil water content is a key limitation factor on vegetation growth. The K_s can also affect both soil moisture and SIF simulations but with reduced magnitude. The wilting point and V_{max} have significant effects on SIF simulation, but their effects on soil moisture simulation are not substantial compared with the B parameter and K_s. Consistent with the previous study (Qiu et al., 2018) in SSiB2/SIF, the wilting point plays a role in connecting the carbon and water cycles in semiarid regions in SSiB4/TRIFFID/SIF. For humid regions, the role of the wilting point is limited, and V_{max} is more important in SIF simulation, especially for the boreal forests.

To evaluate the model performance in predicting the temporal variability of soil moisture and SIF, we created the time series of the monthly satellite observations and simulations in the control run and four tests with the optimal parameter values. Figure 11 demonstrates the monthly mean soil moisture and SIF at the global scale in the control run and the test runs together with the satellite observations from Jan 2016 to Dec 2019. After calibrating the four parameters, the simulated global mean soil moisture increased by about 0.02 $m^3/m^{3,}$ and the simulated global mean SIF decreased by about 0.05 $W/m^2/\mu m/sr$. Among all the PFTs, the seasonality of soil moisture and SIF simulations for C_4 plants and shrubs was best simulated, and the simulated soil moisture and SIF values got the most improvement for these two PFTs (Figure 12). At the global scale, the most improvements in soil moisture were in Test 1 opt, and secondarily in Test 2 opt. The seasonality of soil moisture had a marginal change in four tests, and the increment happened throughout the year. The improved soil moisture simulation still has a considerable discrepancy compared with the SMAP L3 soil moisture, which means the model

needs to be further improved. To pursue more improvement, forthcoming work can use the global high-resolution dataset of soil hydraulic properties instead of parameterization for each vegetation type in the soil moisture simulation (Dai et al., 2019). For the SIF simulation, the most improvement happened in Test 1 opt and Test 4 opt. The SIF simulation was improved in spring, fall, and winter, but got worse in summer. The higher B parameter value decreased the SIF simulation in each season while the change in V_{max} had more effect in summer. To improve

632 the seasonality of SIF simulation, future work can test the parameters in the TRIFFID model to
633 better simulate vegetation distribution, LAI, and SIF.

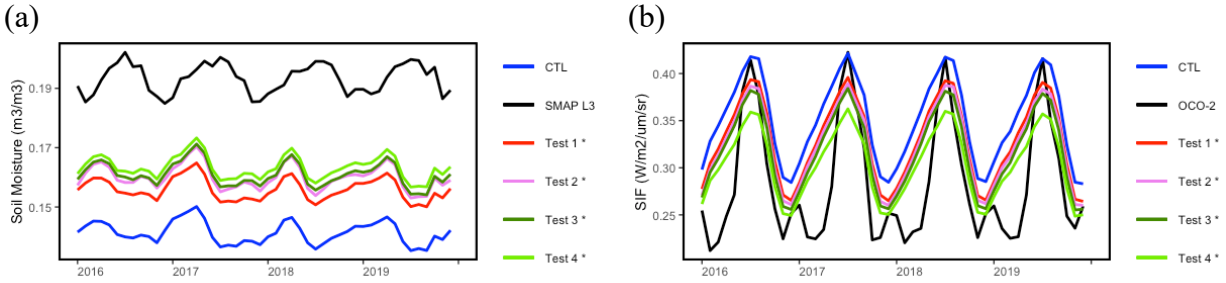

634

635 **Figure 11.** The monthly mean (a) soil moisture and (b) SIF at the global scale (60°S–60°N) in
636 different experiments. * Indicates significant differences between different experiments
637 ($p<0.01$).

638

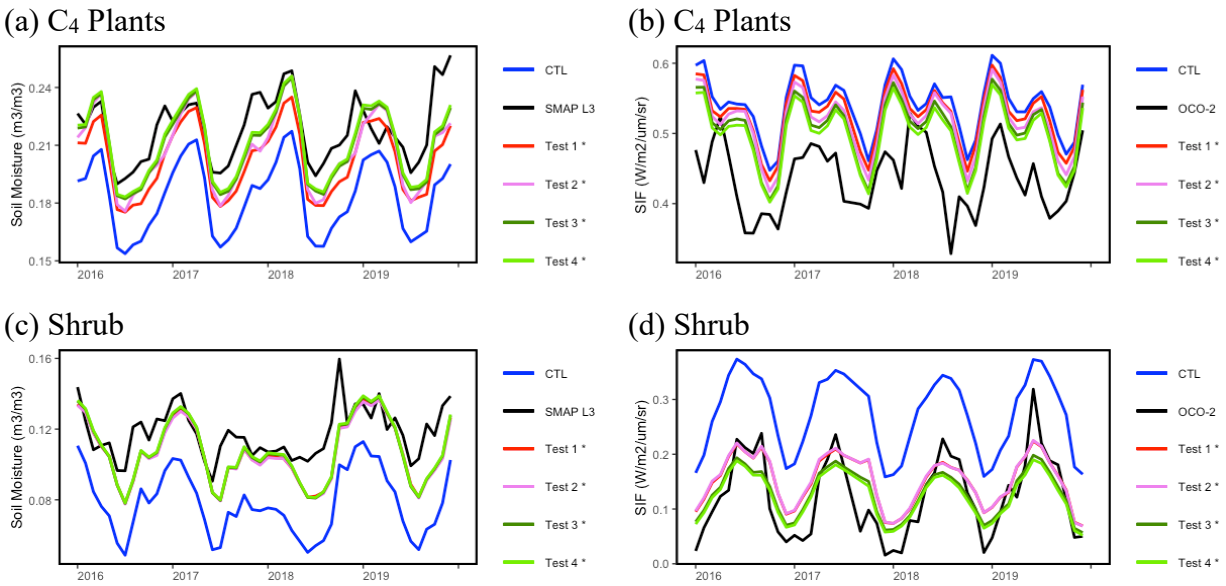

639

640 **Figure 12.** The monthly mean (a, c) soil moisture and (b, d) SIF of (a, b) C_4 plants in Africa and
641 (c, d) shrubs in the Western United States in different experiments. * Indicates significant
642 differences between different experiments ($p<0.01$).

643

644 Qiu et al. (2018) integrated the SMOS soil moisture data and GOSAT SIF data into
645 SSiB2/SIF to understand the response of SIF to soil moisture dynamics. SSiB2/SIF largely
646 overestimated the soil moisture and underestimated the SIF in most regions when evaluated
647 against SMOS soil moisture and GOSAT SIF but underestimated both soil moisture and SIF in
648 semiarid regions. Therefore, calibration of the B parameter and K_s in SSiB2/SIF based on the
649 SMOS soil moisture resulted in better soil moisture simulation but poorer SIF simulation for
650 regions covered by savanna, grass, and shrub. Ma et al. (2019) assessed several satellite surface
651 soil moisture products using global ground-based observations and found that the SMOS
652 products exhibited dry bias due to their underestimating surface temperature. In this study, we
653 used SMAP L3 soil moisture data instead of SMOS to calibrate the B parameter and K_s, and the
654 SIF simulation was evaluated against OCO-2 SIF data. Compared with the SMAP L3 product,
655 SSiB4/TRIFFID/SIF underestimated the soil moisture in most regions. Also, the introduction of
656 the dynamic vegetation processes made the SIF simulation higher than the satellite observation
657 throughout the globe. These two aspects lead to improved soil moisture and SIF simulation in
658 SSiB4/TRIFFID/SIF after calibrating the B parameter and K_s in semiarid regions, which differs
659 from the previous results (Qiu et al., 2018). This study confirmed the importance of using
660 satellite products with higher accuracy and precision, and better spatial and temporal resolution
661 in the calibration of parameters in SSiB models and the exploration of the relationship between
662 soil moisture and SIF. The SMAP products provide the high-resolution mapping of global soil
663 moisture and have been widely validated against core validation sites (Burgin et al., 2017; Zhang
664 et al., 2017). Zhang et al. (2019) assessed the SMAP L3 product using extensive ground
665 measurements from sparse networks and found that the product showed better performance in
666 temperate zones and grassland while negative bias in tropical climate zones and regions with
667 high soil organic carbon contents. As for the OCO-2 SIF data, despite its high resolution, the
668 satellite-observed SIF soundings are sparse, and we averaged the soundings in each 1°×1° pixel
669 first to fulfill more grids with SIF retrieval. This methodology can induce uncertainties in the
670 evaluation of SIF simulation. Those uncertainties in satellite observations can affect the
671 parameter calibration and the understanding of water-carbon cycle interactions. The SMAP L4
672 product assimilates SMAP brightness temperature observations into a land surface model and
673 provides both the 0-5 cm vertical averaged surface soil moisture and the 0-100 cm vertical

674 averaged root zone soil moisture with complete spatial coverage. The Sentinel-5
675 Precursor/TROPOspheric Monitoring Instrument (TROPOMI) launched in 2017 provides SIF
676 data with comparable quality but with largely improved spatial and temporal coverage, and
677 Köhler et al. (2018) suggested tying TROPOMI to OCO-2 SIF data in overlapped regions to
678 virtually fill the large gaps left by the OCO-2 product. Future work can include the SMAP L4
679 and TROPOMI products as further constraints in the model simulation improvement and the
680 SIF–soil moisture relationship exploration.

681 This study was conducted by the offline models, SSiB2/SIF and SSiB4/TRIFFID/SIF,
682 using meteorological forcing to drive soil moisture, SIF, and GPP simulation. With the coupling
683 of the dynamic vegetation model, SSiB4/TRIFFID/SIF can reproduce the global distribution of
684 dominant vegetation types, the vegetation fraction, and the LAI, including its seasonal,
685 interannual, and decadal variabilities (Zhang et al., 2015; Liu et al., 2019), and can provide an
686 improved simulation of photosynthesis and carbon flux. However, the offline model simulation
687 is not able to include feedback to the atmosphere, which represents a lack of investigation on
688 fully coupled two-way interaction. The simulated SIF and GPP in SSiB4/TRIFFID/SIF were
689 much higher than that in SSiB2/SIF, which indicated higher transpiration. Since the same
690 meteorological forcing was used, the simulated total evapotranspiration fluxes in the two models
691 are consistent, with a lower simulated soil evaporation rate in SSiB4/TRIFFID/SIF. The higher
692 vegetation fraction, LAI, transpiration, and photosynthesis rates in SSiB4/TRIFFID/SIF cannot
693 lead to an obvious change in the soil moisture simulation. Zhang et al. (2021) coupled the SSiB2
694 model and the SSiB4/TRIFFID model to the NCEP Global Forecast System (GFS) to investigate
695 vegetation-atmosphere feedback and found that the correlations between the simulated and
696 observed monthly LAI, albedo, near-surface temperature, and precipitation were improved with
697 the dynamic vegetation processes included. Therefore, it remains necessary to add the SIF
698 module into the coupled GFS/SSiB4/TRIFFID model and to evaluate the soil moisture, SIF, and
699 GPP simulated by it against satellite products. This fully coupled biophysical processes model
700 has the potential to better reproduce the satellite-observed soil moisture and carbon flux and to

contribute to the understanding of the interactions between water and carbon cycles through controls over evapotranspiration, vegetation phenology, and surface energy balance.

5 Conclusions

To investigate the role of dynamic vegetation processes on soil moisture and carbon flux simulations and to better understand the relationship between terrestrial carbon and soil moisture dynamics, this study incorporated the SIF module used in SSiB2/SIF into SSiB4/TRIFFID. The soil moisture, SIF, SIF−soil moisture relationship, and GPP simulated by SSiB2/SIF and SSiB4/TRIFFID/SIF were evaluated against the SMAP L3 soil moisture data and the OCO-2 SIF data. The three soil property parameters, the B parameter, K_s, and wilting point, and the vegetation parameter, V_{max}, were tested within the normal range to confirm their important role in the water and carbon cycles in model simulation and to test their effects on soil moisture, SIF, and the interactions. The four parameters were calibrated using the SMAP L3 soil moisture and OCO-2 SIF to improve the soil moisture and SIF simulations in SSiB4/TRIFFID/SIF.

The coupling with the dynamic vegetation model, TRIFFID, led to substantial improvement in the SIF and GPP simulations. The global spatial correlation of SIF increased by 10%, and the global RMSE of SIF simulation decreased by 12%. The global mean GPP simulation increased from 533.2 g C/m^2/yr to 875.2 g C/m^2/yr, which is closer to the median of three observation-based GPP products (867.3 g C/m^2/yr). The global spatial distribution of the correlation coefficient between soil moisture and SIF was more properly simulated in SSiB4/TRIFFID/SIF, with the relationship switched from negative to positive over the Eurasian Steppe and coastal Australia.

The empirical coefficient, B parameter, has the largest impact on soil moisture simulation and efficiently affects the SIF simulation for plants in semi-arid regions through its effects on water potential and soil water diffusion. K_s also affects soil moisture and SIF simulation through the water diffusion in soil layers. The wilting point and V_{max} affect the stomatal opening and the

727 photosynthesis process, thus changing the transpiration rates and SIF simulation. Their effects
728 on soil moisture simulation exist but are less in magnitude than the B parameter and K_s.

729 The SMAP L3 and OCO-2 products improved soil moisture and SIF measurements with
730 better quality, higher spatial and temporal resolution, and accuracy. They can help to improve
731 the global performance of SSiB4/TRIFFID/SIF on soil moisture and SIF simulations and provide
732 advances in understanding the global terrestrial coupled water-carbon cycles. The global RMSE
733 of soil moisture and SIF decreased from 0.076 to 0.067 m^3/m^3 and from 0.143 to 0.129
734 $W/m^2/\mu m/sr$ with the B parameter optimization and further decreased to 0.063 m^3/m^3 and 0.125
735 $W/m^2/\mu m/sr$ with the K_s and wilting point optimized. Calibration of V_{max} further improved the
736 SIF simulation, with the global RMSE decreased to 0.117 $W/m^2/\mu m/sr$.

737

738 **Acknowledgments**

739 This work was supported by NASA grant 19-SMAP19-0018. The authors acknowledge the
740 Land Surface Hydrology Research Group of Princeton University and the European Centre for
741 Medium-Range Weather Forecasts (ECMWF) for providing the meterorological forcing dataset.
742 The data are available at https://rda.ucar.edu/datasets/ds314.0/dataaccess/ and
743 https://cds.climate.copernicus.eu/cdsapp#!/dataset/10.24381/cds.20d54e34?tab=form. The
744 SMAP L3 surface soil moisture data are available at https://nsidc.org/data/spl3smap/versions/3,
745 and the OCO-2 SIF data are available at
746 https://disc.gsfc.nasa.gov/datasets/OCO2_L2_Lite_SIF_10r/summary?keywords=OCO-2. The
747 GLASS GPP data are available at http://www.glass.umd.edu/GPP/AVHRR/, the FLUXCOM
748 GPP data are available at https://www.bgc-jena.mpg.de/geodb/projects/Data.php, and the
749 FLUXSAT GPP data are available at https://daac.ornl.gov/cgi-bin/dsviewer.pl?ds_id=1835.
750

751 **References**

752 Bacour, C., Maignan, F., MacBean, N., Porcar-Castell, A., Flexas, J., Frankenberg, C., ... &
753 Bastrikov, V. (2019). Improving estimates of gross primary productivity by assimilating solar-
754 induced fluorescence satellite retrievals in a terrestrial biosphere model using a process-based

SIF model. *Journal of Geophysical Research: Biogeosciences, 124*(11), 3281–3306. https://doi.org/10.1029/2019JG005040

Bartholome, E., & Belward, A. S. (2005). GLC2000: a new approach to global land cover mapping from Earth observation data. *International Journal of Remote Sensing, 26*(9), 1959–1977. https://doi.org/10.1080/01431160412331291297

Beck, H. E., Pan, M., Miralles, D. G., Reichle, R. H., Dorigo, W. A., Hahn, S., ... & Wood, E. F. (2021). Evaluation of 18 satellite-and model-based soil moisture products using in situ measurements from 826 sensors. *Hydrology and Earth System Sciences, 25*(1), 17–40. https://doi.org/10.5194/hess-25-17-2021

Beerling, D. J., & Quick, W. P. (1995). A new technique for estimating rates of carboxylation and electron transport in leaves of C3 plants for use in dynamic global vegetation models. *Global Change Biology, 1*(4), 289–294. https://doi.org/10.1111/j.1365-2486.1995.tb00027.x

Bhark, E. W., & Small, E. E. (2003). Association between plant canopies and the spatial patterns of infiltration in shrubland and grassland of the Chihuahuan Desert, New Mexico. *Ecosystems, 6*, 0185–0196. https://doi.org/10.1007/s10021-002-0210-9

Bonan, G. B., Lawrence, P. J., Oleson, K. W., Levis, S., Jung, M., Reichstein, M., ... & Swenson, S. C. (2011). Improving canopy processes in the Community Land Model version 4 (CLM4) using global flux fields empirically inferred from FLUXNET data. *Journal of Geophysical Research: Biogeosciences*, *116*(G2). https://doi.org/10.1029/2010JG001593

Clapp, R. B., & Hornberger, G. M. (1978). Empirical equations for some soil hydraulic properties. *Water resources research, 14*(4), 601–604. https://doi.org/10.1029/WR014i004p00601

Clark, D. B., Mercado, L. M., Sitch, S., Jones, C. D., Gedney, N., Best, M. J., ... & Cox, P. M. (2011). The Joint UK Land Environment Simulator (JULES), model description–Part 2: carbon fluxes and vegetation dynamics. *Geoscientific Model Development*, *4*(3), 701–722. https://doi.org/10.5194/gmd-4-701-2011

Collatz, G. J., Ball, J. T., Grivet, C., & Berry, J. A. (1991). Physiological and environmental regulation of stomatal conductance, photosynthesis and transpiration: a model that includes a

783 laminar boundary layer. *Agricultural and Forest meteorology*, *54*(2-4), 107–136.
784 https://doi.org/10.1016/0168-1923(91)90002-8

785 Collatz, G. J., Ribas-Carbo, M., & Berry, J. A. (1992). Coupled photosynthesis-stomatal
786 conductance model for leaves of C4 plants. *Functional Plant Biology*, *19*(5), 519–538.
787 https://doi.org/10.1071/PP9920519

788 Colliander, A., Jackson, T. J., Bindlish, R., Chan, S., Das, N., Kim, S. B., ... & Yueh, S. (2017).
789 Validation of SMAP surface soil moisture products with core validation sites. *Remote sensing of*
790 *environment*, *191*, 215–231. https://doi.org/10.1016/j.rse.2017.01.021

791 Cox, P. M., Betts, R. A., Jones, C. D., Spall, S. A., & Totterdell, I. J. (2000). Acceleration of
792 global warming due to carbon-cycle feedbacks in a coupled climate model. *Nature*, *408*(6809),
793 184–187. https://doi.org/10.1038/35041539

794 Cox, P. M. (2001). Description of the "TRIFFID" dynamic global vegetation model. *Hadley*
795 *Centre Technical Note, 24*, 1–16.

796 Cox, P. M., Betts, R. A., Betts, A., Jones, C. D., Spall, S. A., & Totterdell, I. J. (2002).
797 Modelling vegetation and the carbon cycle as interactive elements of the climate system.
798 *International Geophysics*, *83*, 259–279. https://doi.org/10.1016/S0074-6142(02)80172-3

799 Cox, P. M., Betts, R. A., Collins, M., Harris, P. P., Huntingford, C., & Jones, C. D. (2004).
800 Amazonian forest dieback under climate-carbon cycle projections for the 21st century.
801 *Theoretical and applied climatology*, *78*, 137–156. https://doi.org/10.1007/s00704-004-0049-4

802 Cucchi M., Weedon G. P., Amici A., Bellouin N., Lange S., Müller Schmied H., Hersbach H.,
803 Cagnazzo, C., & Buontempo C. (2022). Near surface meteorological variables from 1979 to
804 2019 derived from bias-corrected reanalysis, version 2.1. Copernicus Climate Change Service
805 (C3S) Climate Data Store (CDS).

806 Dai, Y., Xin, Q., Wei, N., Zhang, Y., Shangguan, W., Yuan, H., ... & Lu, X. (2019). A global
807 high-resolution data set of soil hydraulic and thermal properties for land surface
808 modeling. *Journal of Advances in Modeling Earth Systems*, *11*(9), 2996-3023.
809 https://doi.org/10.1029/2019MS001784

Demaria, E. M., Nijssen, B., & Wagener, T. (2007). Monte Carlo sensitivity analysis of land surface parameters using the Variable Infiltration Capacity model. *Journal of Geophysical Research: Atmospheres*, *112*(D11). https://doi.org/10.1029/2006JD007534

D'Odorico, P., Caylor, K., Okin, G. S., & Scanlon, T. M. (2007). On soil moisture–vegetation feedbacks and their possible effects on the dynamics of dryland ecosystems. *Journal of Geophysical Research: Biogeosciences*, *112*(G4). https://doi.org/10.1029/2006JG000379

Dorman, J. L., & Sellers, P. J. (1989). A global climatology of albedo, roughness length and stomatal resistance for atmospheric general circulation models as represented by the Simple Biosphere Model (SiB). *Journal of Applied Meteorology and Climatology*, *28*(9), 833–855. https://doi.org/10.1175/1520-0450(1989)028<0833:AGCOAR>2.0.CO;2

Doughty, R., Kurosu, T. P., Parazoo, N., Köhler, P., Wang, Y., Sun, Y., & Frankenberg, C. (2022). Global GOSAT, OCO-2, and OCO-3 solar-induced chlorophyll fluorescence datasets. *Earth System Science Data*, *14*(4), 1513–1529. https://doi.org/10.5194/essd-14-1513-2022

Entekhabi, D., Njoku, E. G., O'Neill, P. E., Kellogg, K. H., Crow, W. T., Edelstein, W. N., ... & Van Zyl, J. (2010). The soil moisture active passive (SMAP) mission. *Proceedings of the IEEE*, *98*(5), 704–716. 10.1109/JPROC.2010.2043918

Font, J., Kerr, Y. H., Srokosz, M. A., Etcheto, J., Lagerloef, G. S., Camps, A., & Waldteufel, P. (2001, January). SMOS: A satellite mission to measure ocean surface salinity. In *Atmospheric Propagation, Adaptive Systems, and Laser Radar Technology for Remote Sensing* (Vol. 4167, pp. 207–214). SPIE. https://doi.org/10.1117/12.413825

Frankenberg, C., Fisher, J. B., Worden, J., Badgley, G., Saatchi, S. S., Lee, J. E., ... & Yokota, T. (2011). New global observations of the terrestrial carbon cycle from GOSAT: Patterns of plant fluorescence with gross primary productivity. *Geophysical Research Letters*, *38*(17). https://doi.org/10.1029/2011GL048738

Gonsamo, A., Chen, J. M., He, L., Sun, Y., Rogers, C., & Liu, J. (2019). Exploring SMAP and OCO-2 observations to monitor soil moisture control on photosynthetic activity of global drylands and croplands. *Remote Sensing of Environment*, *232*, 111314. https://doi.org/10.1016/j.rse.2019.111314

838 Harper, A. B., Cox, P. M., Friedlingstein, P., Wiltshire, A. J., Jones, C. D., Sitch, S., ... &
839 Bodegom, P. V. (2016). Improved representation of plant functional types and physiology in the
840 Joint UK Land Environment Simulator (JULES v4. 2) using plant trait information. *Geoscientific*
841 *Model Development*, *9*(7), 2415–2440. https://doi.org/10.5194/gmd-9-2415-2016

842 Hawkins, L. R., Rupp, D. E., McNeall, D. J., Li, S., Betts, R. A., Mote, P. W., ... & Wallom, D.
843 C. (2019). Parametric sensitivity of vegetation dynamics in the TRIFFID model and the
844 associated uncertainty in projected climate change impacts on western US Forests. *Journal of*
845 *Advances in Modeling Earth Systems*, *11*(8), 2787–2813. https://doi.org/10.1029/2018MS001577

846 Helm, L. T., Shi, H., Lerdau, M. T., & Yang, X. (2020). Solar-induced chlorophyll fluorescence
847 and short-term photosynthetic response to drought. *Ecological Applications*, *30*(5), e02101.
848 https://doi.org/10.1002/eap.2101

849 Huang, H., Xue, Y., Li, F., & Liu, Y. (2020). Modeling long-term fire impact on ecosystem
850 characteristics and surface energy using a process-based vegetation–fire model SSiB4/TRIFFID-
851 Fire v1. 0. *Geoscientific Model Development*, *13*(12), 6029–6050. https://doi.org/10.5194/gmd-
852 13-6029-2020

853 Humphrey, V., Berg, A., Ciais, P., Gentine, P., Jung, M., Reichstein, M., ... & Frankenberg, C.
854 (2021). Soil moisture–atmosphere feedback dominates land carbon uptake variability. *Nature*,
855 *592*(7852), 65–69. https://doi.org/10.1038/s41586-021-03325-5

856 Jia, W., Liu, M., Wang, D., He, H., Shi, P., Li, Y., & Wang, Y. (2018). Uncertainty in simulating
857 regional gross primary productivity from satellite-based models over northern China grassland.
858 *Ecological Indicators*, *88*, 134–143. https://doi.org/10.1016/j.ecolind.2018.01.028

859 Joiner, J., Guanter, L., Lindstrot, R., Voigt, M., Vasilkov, A. P., Middleton, E. M., ... &
860 Frankenberg, C. (2013). Global monitoring of terrestrial chlorophyll fluorescence from moderate
861 spectral resolution near-infrared satellite measurements: Methodology, simulations, and
862 application to GOME-2. *Atmospheric Measurement Techniques Discussions*, *6*(2), 3883–3930.
863 https://doi.org/10.5194/amt-6-2803-2013

864 Joiner, J., and Y. Yoshida. (2020). Satellite-based reflectances capture large fraction of
865 variability in global gross primary production (GPP) at weekly time scales. *Agricultural and*
866 *Forest Meteorology 291*:108092. https://doi.org/10.1016/j.agrformet.2020.108092

867 Joiner, J., and Y. Yoshida. (2021). Global MODIS and FLUXNET-derived Daily Gross Primary
868 Production, V2. ORNL DAAC, Oak Ridge, Tennessee,
869 USA. https://doi.org/10.3334/ORNLDAAC/1835

870 Jonard, F., Feldman, A. F., Short Gianotti, D. J., & Entekhabi, D. (2022). Observed water and
871 light limitation across global ecosystems. *Biogeosciences*, *19*(23), 5575–5590.
872 https://doi.org/10.5194/bg-19-5575-2022

873 Kang, H. S., Xue, Y., & Collatz, G. J. (2007). Impact assessment of satellite-derived leaf area
874 index datasets using a general circulation model. *Journal of climate*, *20*(6), 993–1015.
875 https://doi.org/10.1175/JCLI4054.1

876 Kattge, J., Knorr, W., Raddatz, T., & Wirth, C. (2009). Quantifying photosynthetic capacity and
877 its relationship to leaf nitrogen content for global-scale terrestrial biosphere models. *Global*
878 *Change Biology*, *15*(4), 976–991. https://doi.org/10.1111/j.1365-2486.2008.01744.x

879 Kerr, Y. H., Waldteufel, P., Richaume, P., Wigneron, J. P., Ferrazzoli, P., Mahmoodi, A., ... &
880 Delwart, S. (2012). The SMOS soil moisture retrieval algorithm. *IEEE transactions on*
881 *geoscience and remote sensing*, *50*(5), 1384–1403. 10.1109/TGRS.2012.2184548

882 Kim, Y., & Wang, G. (2012). Soil moisture-vegetation-precipitation feedback over North
883 America: Its sensitivity to soil moisture climatology. *Journal of Geophysical Research:*
884 *Atmospheres*, *117*(D18). https://doi.org/10.1029/2012JD017584

885 Köhler, P., Frankenberg, C., Magney, T. S., Guanter, L., Joiner, J., & Landgraf, J. (2018). Global
886 retrievals of solar-induced chlorophyll fluorescence with TROPOMI: First results and intersensor
887 comparison to OCO-2. *Geophysical Research Letters*, *45*(19), 10-456.
888 https://doi.org/10.1029/2018GL079031

889 Koster, R. D., Chang, Y., Wang, H., & Schubert, S. D. (2016). Impacts of local soil moisture
890 anomalies on the atmospheric circulation and on remote surface meteorological fields during
891 boreal summer: A comprehensive analysis over North America. *Journal of Climate*, *29*(20),
892 7345–7364. https://doi.org/10.1029/2012JD017584

893 Lee, J. E., Berry, J. A., van der Tol, C., Yang, X., Guanter, L., Damm, A., ... & Frankenberg, C.
894 (2015). Simulations of chlorophyll fluorescence incorporated into the Community Land Model
895 version 4. *Global Change Biology*, *21*(9), 3469–3477. https://doi.org/10.1111/gcb.12948

Leng, S., Huete, A., Cleverly, J., Gao, S., Yu, Q., Meng, X., ... & Wang, Q. (2022). Assessing the impact of extreme droughts on dryland vegetation by multi-satellite solar-induced chlorophyll fluorescence. *Remote Sensing*, *14*(7), 1581. https://doi.org/10.3390/rs14071581

Le Quéré, C., Andrew, R. M., Canadell, J. G., Sitch, S., Korsbakken, J. I., Peters, G. P., ... & Zaehle, S. (2016). Global carbon budget 2016. *Earth System Science Data*, *8*(2), 605–649. https://doi.org/10.5194/essd-8-605-2016

Levis, S., & Bonan, G. B. (2004). Simulating springtime temperature patterns in the community atmosphere model coupled to the community land model using prognostic leaf area. *Journal of Climate*, *17*(23), 4531–4540. https://doi.org/10.1175/3218.1

Li, X., Liang, S., Yu, G., Yuan, W., Cheng, X., Xia, J., ... & Kato, T. (2013). Estimation of gross primary production over the terrestrial ecosystems in China. *Ecological Modelling*, *261*, 80–92. https://doi.org/10.1016/j.ecolmodel.2013.03.024

Li, X., Xiao, J., He, B., Altaf Arain, M., Beringer, J., Desai, A. R., ... & Varlagin, A. (2018). Solar-induced chlorophyll fluorescence is strongly correlated with terrestrial photosynthesis for a wide variety of biomes: First global analysis based on OCO-2 and flux tower observations. *Global Change Biology*, *24*(9), 3990–4008. https://doi.org/10.1111/gcb.14297

Liu, L., Gudmundsson, L., Hauser, M., Qin, D., Li, S., & Seneviratne, S. I. (2020). Soil moisture dominates dryness stress on ecosystem production globally. *Nature communications*, *11*(1), 4892. https://doi.org/10.1038/s41467-020-18631-1

Lu, L., Pielke Sr, R. A., Liston, G. E., Parton, W. J., Ojima, D., & Hartman, M. (2001). Implementation of a two-way interactive atmospheric and ecological model and its application to the central United States. *Journal of Climate*, *14*(5), 900–919. https://doi.org/10.1175/1520-0442(2001)014<0900:IOATWI>2.0.CO;2

Ma, H., Zeng, J., Chen, N., Zhang, X., Cosh, M. H., & Wang, W. (2019). Satellite surface soil moisture from SMAP, SMOS, AMSR2 and ESA CCI: A comprehensive assessment using global ground-based observations. *Remote Sensing of Environment*, *231*, 111215. https://doi.org/10.1016/j.rse.2019.111215

923 Manzoni, S., Vico, G., Palmroth, S., Porporato, A., & Katul, G. (2013). Optimization of stomatal
924 conductance for maximum carbon gain under dynamic soil moisture. *Advances in Water*
925 *Resources*, *62*, 90–105. https://doi.org/10.1016/j.advwatres.2013.09.020

926 McColl, K. A., Alemohammad, S. H., Akbar, R., Konings, A. G., Yueh, S., & Entekhabi, D.
927 (2017). The global distribution and dynamics of surface soil moisture. *Nature Geoscience*, *10*(2),
928 100–104. https://doi.org/10.1038/ngeo2868

929 Niyogi, D., & Xue, Y. (2006). Soil moisture regulates the biological response of elevated
930 atmospheric CO2 concentrations in a coupled atmosphere biosphere model. *Global and*
931 *Planetary Change*, *54*(1-2), 94–108. https://doi.org/10.1016/j.gloplacha.2006.02.016

932 Njoku, E. G., Jackson, T. J., Lakshmi, V., Chan, T. K., & Nghiem, S. V. (2003). Soil moisture
933 retrieval from AMSR-E. *IEEE Transactions on Geoscience and Remote Sensing*, *41*(2), 215–
934 229. 10.1109/TGRS.2002.808243

935 O'Neill, P., Chan, S., Bindlish, R., Chaubell, M., Colliander, A., Chen, F., ... & Starks14, P.
936 (2020). *Soil Moisture Active Passive (SMAP) Project: Calibration and Validation for the*
937 *L2/3_SM_P Version 7 and L2/3_SM_P_E Version 4 Data Products* (pp. 1–44). Technical Report
938 JPL D-56297.

939 Piao, S., Fang, J., Ciais, P., Peylin, P., Huang, Y., Sitch, S., & Wang, T. (2009). The carbon
940 balance of terrestrial ecosystems in China. *Nature*, *458*(7241), 1009–1013.
941 https://doi.org/10.1038/nature07944

942 Piao, S., Sitch, S., Ciais, P., Friedlingstein, P., Peylin, P., Wang, X., ... & Zeng, N. (2013).
943 Evaluation of terrestrial carbon cycle models for their response to climate variability and to CO2
944 trends. *Global Change Biology*, *19*(7), 2117–2132. https://doi.org/10.1111/gcb.12187

945 Porcar-Castell, A., Tyystjärvi, E., Atherton, J., Van der Tol, C., Flexas, J., Pfündel, E. E., ... &
946 Berry, J. A. (2014). Linking chlorophyll a fluorescence to photosynthesis for remote sensing
947 applications: mechanisms and challenges. *Journal of Experimental Botany*, *65*(15), 4065–4095.
948 https://doi.org/10.1093/jxb/eru191

949 Prihodko, L., Denning, A. S., Hanan, N. P., Baker, I., & Davis, K. (2008). Sensitivity,
950 uncertainty and time dependence of parameters in a complex land surface model. *Agricultural*
951 *and Forest Meteorology*, *148*(2), 268–287. https://doi.org/10.1016/j.agrformet.2007.08.006

Qiu, B., Xue, Y., Fisher, J. B., Guo, W., Berry, J. A., & Zhang, Y. (2018). Satellite chlorophyll fluorescence and soil moisture observations lead to advances in the predictive understanding of global terrestrial coupled carbon-water cycles. *Global Biogeochemical Cycles*, *32*(3), 360–375. https://doi.org/10.1002/2017GB005744

Qiu, B., Ge, J., Guo, W., Pitman, A. J., & Mu, M. (2020). Responses of Australian dryland vegetation to the 2019 heat wave at a subdaily scale. *Geophysical Research Letters*, *47*(4), e2019GL086569. https://doi.org/10.1029/2019GL086569

Scholze, M., Kaminski, T., Knorr, W., Blessing, S., Vossbeck, M., Grant, J. P., & Scipal, K. (2016). Simultaneous assimilation of SMOS soil moisture and atmospheric CO2 in-situ observations to constrain the global terrestrial carbon cycle. *Remote Sensing of Environment*, *180*, 334–345. https://doi.org/10.1016/j.rse.2016.02.058

Sellers, P. J., Tucker, C. J., Collatz, G. J., Los, S. O., Justice, C. O., Dazlich, D. A., & Randall, D. A. (1996). A revised land surface parameterization (SiB2) for atmospheric GCMs. Part II: The generation of global fields of terrestrial biophysical parameters from satellite data. *Journal of Climate, 9*(4), 706-737. https://doi.org/10.1175/1520-0442(1996)009<0706:ARLSPF>2.0.CO;2

Seneviratne, S. I., Corti, T., Davin, E. L., Hirschi, M., Jaeger, E. B., Lehner, I., ... & Teuling, A. J. (2010). Investigating soil moisture–climate interactions in a changing climate: A review. *Earth-Science Reviews*, *99*(3-4), 125–161. https://doi.org/10.1016/j.earscirev.2010.02.004

Sheffield, J., Goteti, G., & Wood, E. F. (2006). Development of a 50-year high-resolution global dataset of meteorological forcings for land surface modeling. *Journal of Climate*, *19*(13), 3088–3111. https://doi.org/10.1175/JCLI3790.1

Short Gianotti, D. J., Rigden, A. J., Salvucci, G. D., & Entekhabi, D. (2019). Satellite and station observations demonstrate water availability's effect on continental-scale evaporative and photosynthetic land surface dynamics. *Water Resources Research*, *55*(1), 540–554. https://doi.org/10.1029/2018WR023726

Sitch, S., Huntingford, C., Gedney, N., Levy, P. E., Lomas, M., Piao, S. L., ... & Woodward, F. I. (2008). Evaluation of the terrestrial carbon cycle, future plant geography and climate-carbon

cycle feedbacks using five Dynamic Global Vegetation Models (DGVMs). *Global Change Biology*, *14*(9), 2015–2039. https://doi.org/10.1111/j.1365-2486.2008.01626.x

Sun, Y., Frankenberg, C., Wood, J. D., Schimel, D. S., Jung, M., Guanter, L., ... & Yuen, K. (2017). OCO-2 advances photosynthesis observation from space via solar-induced chlorophyll fluorescence. *Science, 358*(6360), eaam5747. 10.1126/science.aam5747

Sun, Y., Frankenberg, C., Jung, M., Joiner, J., Guanter, L., Köhler, P., & Magney, T. (2018). Overview of Solar-Induced chlorophyll Fluorescence (SIF) from the Orbiting Carbon Observatory-2: Retrieval, cross-mission comparison, and global monitoring for GPP. *Remote Sensing of Environment*, *209*, 808–823. https://doi.org/10.1016/j.rse.2018.02.016

Tolk, J. A. (2003). Soils, permanent wilting points. *Encyclopedia of Water Science*, *120010337,* 92. 10.1081/E-EWS 120010337

Tramontana, G., Jung, M., Schwalm, C. R., Ichii, K., Camps-Valls, G., Ráduly, B., ... & Papale, D. (2016). Predicting carbon dioxide and energy fluxes across global FLUXNET sites with regression algorithms. *Biogeosciences*, *13*(14), 4291–4313. https://doi.org/10.5194/bg-13-4291-2016

Von Caemmerer S., & Furbank R. T. (1999). Modeling C4 photosynthesis. In: Sage R. F., Monson R. K. (Eds.), *C4 Plant Biology* (pp. 173–211). San Diego, CA: Academic.

Walker, B. H., Ludwig, D., Holling, C. S., & Peterman, R. M. (1981). Stability of semi-arid savanna grazing systems. *The Journal of Ecology*, 473–498. https://doi.org/10.2307/2259679

Walther, S., Voigt, M., Thum, T., Gonsamo, A., Zhang, Y., Köhler, P., ... & Guanter, L. (2016). Satellite chlorophyll fluorescence measurements reveal large-scale decoupling of photosynthesis and greenness dynamics in boreal evergreen forests. *Global Change Biology*, *22*(9), 2979–2996. https://doi.org/10.1111/gcb.13200

Wang, J., Jiang, F., Wang, H., Qiu, B., Wu, M., He, W., ... & Zhou, Y. (2021). Constraining global terrestrial gross primary productivity in a global carbon assimilation system with OCO-2 chlorophyll fluorescence data. *Agricultural and Forest Meteorology*, *304*, 108424. https://doi.org/10.1016/j.agrformet.2021.108424

Wigneron, J. P., Jackson, T. J., O'neill, P., De Lannoy, G., de Rosnay, P., Walker, J. P., ... & Kerr, Y. (2017). Modelling the passive microwave signature from land surfaces: A review of

recent results and application to the L-band SMOS & SMAP soil moisture retrieval algorithms. *Remote Sensing of Environment*, *192*, 238–262. https://doi.org/10.1016/j.rse.2017.01.024

Wu, M., Scholze, M., Kaminski, T., Voßbeck, M., & Tagesson, T. (2020). Using SMOS soil moisture data combining CO2 flask samples to constrain carbon fluxes during 2010–2015 within a Carbon Cycle Data Assimilation System (CCDAS). *Remote Sensing of Environment*, *240*, 111719. https://doi.org/10.1016/j.rse.2020.111719

Wullschleger, S. D. (1993). Biochemical limitations to carbon assimilation in C3 plants—a retrospective analysis of the A/Ci curves from 109 species. *Journal of Experimental Botany*, *44*(5), 907–920. https://doi.org/10.1093/jxb/44.5.907

Xue, Y. (1991). A two-dimensional coupled biosphere-atmosphere model and its application. *Advances in atmospheric sciences*, *8*(4), 447-458. https://doi.org/10.1007/BF02919267

Xue, Y., Juang, H. M., Li, W. P., Prince, S., DeFries, R., Jiao, Y., & Vasic, R. (2004). Role of land surface processes in monsoon development: East Asia and West Africa. *Journal of Geophysical Research: Atmospheres, 109*(D3). https://doi.org/10.1029/2003JD003556

Xue, Y., Zeng, F. J., & Schlosser, C. A. (1996). SSiB and its sensitivity to soil properties—A case study using HAPEX-Mobilhy data. *Global and Planetary Change*, *13*(1-4), 183–194. https://doi.org/10.1016/0921-8181(95)00045-3

Xue, Y., H. Deng, and P. M. Cox (2006), Testing a coupled biophysical/dynamic vegetation model (SSiB-4/TRIFFID) in different climate zones using satellite-derived and ground-measured data, 86th AMS Annual Meeting, 18th Conference on Climate Variability and Change. [Available at https://ams.confex.com/ams/Annual2006/webprogram/Paper101721.html.]

Yuan, W., Liu, S., Zhou, G., Zhou, G., Tieszen, L. L., Baldocchi, D., ... & Wofsy, S. C. (2007). Deriving a light use efficiency model from eddy covariance flux data for predicting daily gross primary production across biomes. *Agricultural and Forest Meteorology*, *143*(3-4), 189–207. https://doi.org/10.1016/j.agrformet.2006.12.001

Yuan, W., Cai, W., Xia, J., Chen, J., Liu, S., Dong, W., ... & Wohlfahrt, G. (2014). Global comparison of light use efficiency models for simulating terrestrial vegetation gross primary

1037 production based on the LaThuile database. *Agricultural and Forest Meteorology*, *192*, 108–120.
1038 https://doi.org/10.1016/j.agrformet.2014.03.007

1039 Zhan, X., Xue, Y., & Collatz, G. J. (2003). An analytical approach for estimating CO2 and heat
1040 fluxes over the Amazonian region. *Ecological Modelling*, *162*(1-2), 97–117.
1041 https://doi.org/10.1016/S0304-3800(02)00405-2

1042 Zhang, R., Kim, S., & Sharma, A. (2019). A comprehensive validation of the SMAP Enhanced
1043 Level-3 Soil Moisture product using ground measurements over varied climates and landscapes.
1044 *Remote Sensing of Environment*, *223*, 82–94. https://doi.org/10.1016/j.rse.2019.01.015

1045 Zhang, X., Zhang, T., Zhou, P., Shao, Y., & Gao, S. (2017). Validation analysis of SMAP and
1046 AMSR2 soil moisture products over the United States using ground-based measurements.
1047 *Remote Sensing*, *9*(2), 104. https://doi.org/10.3390/rs9020104

1048 Zhang, Y., & Ye, A. (2021). Would the obtainable gross primary productivity (GPP) products
1049 stand up? A critical assessment of 45 global GPP products. *Science of the Total Environment*,
1050 *783*, 146965. https://doi.org/10.1016/j.scitotenv.2021.146965

1051 Zhang, Z., Chatterjee, A., Ott, L., Reichle, R., Feldman, A. F., & Poulter, B. (2022). Effect of
1052 Assimilating SMAP Soil Moisture on CO_2 and CH_4 Fluxes through Direct Insertion in a Land
1053 Surface Model. *Remote Sensing*, *14*(10), 2405. https://doi.org/10.3390/rs14102405

1054 Zhang, Z., Xue, Y., MacDonald, G., Cox, P. M., & Collatz, G. J. (2015). Investigation of North
1055 American vegetation variability under recent climate: A study using the SSiB4/TRIFFID
1056 biophysical/dynamic vegetation model. *Journal of Geophysical Research: Atmospheres*, *120*(4),
1057 1300–1321. https://doi.org/10.1002/2014JD021963

1058 Zhang, Z., Xue, Y., Zhai, P., & Deng, H. (2021). Effects of Dynamic Vegetation on Global
1059 Climate Simulation Using the NCEP GFS and SSiB4/TRIFFID. *Journal of Meteorological*
1060 *Research*, *35*, 1041–1056. https://doi.org/10.1007/s13351-021-1099-6